Seasonal and interannual variations of the Tsushima Warm Current paths in the southwestern part of the Japan Sea

ITO, Masashi

Seasonal and interannual variations of the Tsushima Warm Current paths in the southwestern part of the Japan Sea

（日本海南西海域における対馬暖流の流路の季節経年変化）

ITO, Masashi
（伊藤　雅）

A dissertation for the degree of Doctor of Science
Department of Earth and Environmental Sciences,
Graduate School of Environmental Studies, Nagoya University
（名古屋大学大学院環境学研究科地球環境科学専攻学位論文　博士（理学））

Contents

Abstract · iii
Acknowledgments · viii

1 Introduction **1**

2 Tsushima warm current paths in the Japan Sea **8**

2.1 Introduction · 8
2.2 Data and methods · 9
2.2.1 Calculation of the sea surface current anomaly from altimetry data · · · · · · · · · · 10
2.2.2 Calculation of the mean sea surface current and absolute sea surface current · · · · · · 12
2.2.3 Validation of absolute sea surface current data · · · · · · · · · · · · · · · · · 17
2.3 Results · 19
2.3.1 Mean sea surface current field of the TWC · · · · · · · · · · · · · · · · · · · 19
2.3.2 Seasonal variation in the triple branches of the TWC in the southwestern part of the Japan Sea · 20
2.3.2.1 Method of analysis for seasonal variation in current paths · · · · · · · · · · · · 20
2.3.2.2 Seasonal variation in TWC paths · 22
2.3.2.3 FBTWC and SBTWC paths at the continental shelf · · · · · · · · · · · · · · · 24
2.4 Discussion · 25
2.5 Summary · 28

3 Interannual variation in the TBTWC controlled by winter surface cooling in the Japan Sea – Data analysis - **42**

3.1 Introduction · 42
3.2 Data · 44
3.2.1 Monthly absolute sea surface dynamical height field · · · · · · · · · · · · · · · · 44
3.2.2 Data processing for the other data · 47
3.3 Variations in the TBTWC path · 48
3.3.1 Seasonal and interannual variation in the TWC · · · · · · · · · · · · · · · · · · 48
3.3.2 Variation factor of separation position of the TBTWC from the Korean Peninsula · 51
3.4 Summary · 55

4 Interannual variation in the TBTWC controlled by winter surface cooling in the Japan Sea - Numerical experiment - 68

4.1 Introduction · 68

4.2 Description of the model · 69

4.3 Validation of the Model and variability of current paths from winter to summer · · · · · · 72

4.4 Sensitivity experiments for the winter net heat flux changes · · · · · · · · · · · · · · · 75

4.5 Summary · 79

5 Discussion 90

6 Conclusion 95

References 99

Abstract

Oceanographers have long been interested in and investigated paths of the Tsushima Warm Current (TWC). However, there is no consensus on the pattern of the TWC paths because large- and small-scale eddies cause large variability in the TWC paths and make it difficult to discern the variability in the sea surface current field using ship-observed data.

In the present study, we compiled a long-term record of monthly mean sea surface currents and monthly mean sea surface dynamic heights with high spatial-temporal resolution in the Japan Sea from satellite altimetry and satellite-tracked drifter data. Using these data, we examined paths of the TWC in the southwestern part of the Japan Sea and investigated the variability in the TWC paths.

The mean current paths of the TWC consist of three branches. The first branch through the eastern channel of the Tsushima Strait flows along the Japanese archipelago. The second branch flows along the continental shelf edge around 200-m isobath. The third branch flows along the east coast of the Korean Peninsula. We investigated seasonal variation in the path of each branch by frequency analysis. Seasonal variations in the paths of the first and the third branch are small. While path of the second branch is obscure in November. Although the seasonal variation in the third branch of the TWC

(TBTWC) path is small, interannual variation in the TBTWC path is occasionally large.

Previous studies reported the interannual variation of the TBTWC path. To investigate a factor of the interannual variation in the TBTWC path, empirical orthogonal function (EOF) analysis is applied to the absolute sea surface dynamic height (ASSDH) data. The EOF decomposition of the ASSDH in the southern part of the Japan Sea yields two dominant modes explaining 79% and 9% of the total variance, respectively. The EOF 1st mode shows strong and weak of the TWC with seasonal variation. The largest amplitude exists off east coast of the Korean Peninsula in the EOF 2nd mode, and the variation in this region indicates the variability of the TBTWC path. Interannual variation is dominant in time series of the EOF 2nd mode. The variation of the EOF 2nd mode notably denotes separation position of the TBTWC from the Korean Peninsula.

We examined the cause of interannual variation in the TBTWC path by correlation and lag correlation analysis. A parameter of highest correlation was spatially averaged net heart flux over the northern Japan Sea in winter. This fact suggests that separation position of the TBTWC from the Korean Peninsula moves to more south (north) when the surface cooling in the northern part of the Japan Sea in winter is strong (weak). We also analyzed relationship between the net heat flux over northern Japan Sea and

subarctic circulation in the Japan Sea, and hydrographic condition around east of Koran Peninsula, respectively. Correlation analyses suggest that interannual variation of separation position of the TBTWC relates to strong and weak variation of subarctic circulation. In addition, strong and weak of subarctic circulation in spring might be caused by variation in surface cooling in winter. These results imply the following processes. The subarctic circulation is intensified by stronger winter cooling compared to normal year, and then more amount of cold water mass is transported to off Korean coast by the current. As a result, the cold water mass off Korean coast expand in wider area. The TBTWC adjusts the density distribution off Korean coast and separates from the coast at lower latitude. There might be time lag between intensification of the subarctic circulation current and transport of cold water mass to off Korean coast. Hence it seems that separation position of the TBTWC from spring to summer has high correlation with surface cooling in the northern part of the Japan Sea in winter.

In order to reveal the relationship between variation in strength of surface cooling in winter and strong and weak of subarctic circulation, variation in distribution of cold water mass off Korean coast, and variation in the TBTWC path from spring to summer, we performed numerical experiments using a reduced gravity model with simple topography. We performed the two cases experiment with large winter surface cooling

and non large cooling, respectively. The model results showed that the strength of the spatial gradient of surface cooling in winter controls the separated position of the TBTWC path from spring to summer about 150 km. Separation position of the TBTWC from the Korean Peninsula and water distribution in the numerical model result was consistent with the data analysis of absolute sea surface dynamic height field and ship-observed data.

Relationship between change of separation position of the TBTWC in summer and that of surface cooling in winter is explained as follows. Stronger surface cooling in winter makes increase of upper layer thickness along north coast. The increased upper layer thickness continuously propagates to the west as internal Kelvin wave. As a result, upper layer thickness in the western part of the Japan Sea in strong surface cooling year in winter is deeper than that in normal surface cooling year in winter. Subarctic circulation and North Korean Cold Current were enhanced by the current caused by interfacial gradient by propagating internal Kelvin waves along the Russian coast. Since intensified North Korean Cold Current in strong surface cooling year in winter transports cold water mass to the south along west coast, the cold water spread around the east coast of the Korean Peninsula. The northward current (TBTWC) along west coast flows along the boundary of the lower water distribution and strong sea surface cooling year separates at lower latitude than that in normal sea surface cooling year in summer time. Consequently, it was clear that the variation of the amount of the surface cooling in the northern part of the Japan Sea in winter controlled the separation position of the TBTWC from the Korean Peninsula in summer with a half year time lag by data analysis and numerical experiment.

Acknowledgements

I would like to express sincere and my hearty acknowledgement to my supervisor, Associate Prof. Akihiko Morimoto, Hydrospheric Atmospheric Research Center (HyARC), Nagoya University for his passionate instruction and encouragement. I would like to thank Prof. Joji Ishizaka, Prof. Kazuhisa Tsuboki, HyARC, Nagoya University, and Prof. Naoki Hirose, Research Institute for Applied Mechanics, Kyushu University, for their participation in fruitful discussions and their valuable suggestions. Thanks are also extended to Dr. Hiroyuki Tomita, HyARC, Nagoya University, Dr. Daisuke Takahashi, Tohoku University and members of Laboratory of Bio-Physical Oceanography of HyARC.

Thanks are expected to Associate Prof. Tetsutaro Takikawa, National Fisheries University, for his helpful suggestions and officers and crews of T/Vs Tenyo-maru of National Fisheries University for giving me opportunity for participating the observations. The Japan Sea National Fisheries Research Institute is acknowledged for providing the satellite-tracked buoy data.

Finally, I would like to give my special thanks to my parents of their continuous and patient supports over the years.

Figures were produced by GFD-DENNOU Library.

Chapter 1

Introduction

The Japan Sea is a marginal sea surrounded by the Eurasian continent and the Japanese Archipelago. The maximum water depth is more than 3000 m. Water exchange between the Japan Sea and adjacent seas mainly occurs through the Tsushima Strait, Tsugaru Strait, and Soya Strait, which connect the Japan Sea to the East China Sea, Pacific Ocean, and Okhotsk Sea, respectively (Fig. 1.1). Through these straits, particularly the Tsushima Strait, the Japan Sea receives large amounts of fresh water and nutrients carried by the Tsushima Warm Current (TWC) (Isobe *et al*., 2002; Onitsuka *et al*., 2007; Morimoto *et al*., 2009b). Variability in the path of the TWC in the Japan Sea might affect the transport and distribution of materials such as nutrients and may thus influence biological productivity. Oceanographers have long been interested in the paths of the TWC (Uda, 1934a,b, 1936; Tanioka, 1968; Kawabe, 1982a, b; Katoh, 1993, 1994a, b; Hase *et al*., 1999; Hogan and Hurlburt, 2000; Morimoto and Yanagi, 2001, Morimoto *et al*., 2009a; Mitchell *et al*., 2005; Lee and Niiler, 2005, 2010a, b; Hirose *et al*., 2009; Watanabe *et al*., 2009), and some current patterns have been proposed.

Among these, the “single-meander,” “double-branch,” and “triple-branch” patterns have been traditionally recognized. In the single-meander pattern, the TWC has one path that flows through the western channel of the Tsushima Strait along the east coast of the Korean Peninsula around 38ºN. It then meanders toward the Tsugaru Strait (Tanioka, 1968). In the double-branch pattern, in addition to the northward flow along the east coast of Korea, another current exists along the Japanese archipelago after flowing through the eastern channel of the Tsushima Strait (Hogan and Hurlburt, 2000; Lee and Niiler, 2005). These two current paths are recognized in the triple-branch pattern, in addition to a current that exists around the 200-m isobath at the continental shelf edge after flowing through the western channel of the Tsushima Strait (Kawabe 1982a, b; Katoh, 1994b; Hase *et al*., 1999). In the triple-branch pattern, the current path along the west coast of Japan is called the first branch of the TWC (FBTWC), that along the continental shelf edge is called the second branch of the TWC (SBTWC), and that along the east coast of the Korean Peninsula is called the third branch of the TWC (TBTWC). According to previous studies, the FBTWC is stable currents, the SBTWC exhibits seasonality, and TBTWC is highly stable current as a western boundary current (Kawabe 1982a, b; Hase *et al*., 1999). In the present study, we define these branches as the same name of the triple-branch pattern in the southwestern part of the Japan Sea

(Fig. 1.2).

Tanioka's (1968) analysis of water temperature at 100 m depth supported the single-meander pattern. Lee and Niiler (2005) and Hogan and Hurlburt (2000) reported the double-branch pattern from analyses of satellite-tracked drifters and numerical model results, respectively. The triple-branch pattern was found by Hase *et al*. (1999), Kawabe (1982a, b), Sekine (1986), Katoh (1994b), and Watanabe *et al*. (2009), who investigated the TWC path using observed data and numerical model results.

Moreover, another pattern of TWC paths was proposed by Morimoto *et al*. (2009a). They suggested that two current axes corresponding to the SBTWC and FBTWC appear throughout the year at the continental shelf edge and 100-m isobath. Meanwhile, Hirose *et al*. (2009) proposed another pattern in which one branch flows downstream of the western channel of the Tsushima Strait and two branches flow downstream of the eastern channel of the Tsushima Strait. Moreover, Hong and Cho (1983), Kim and Legeckis (1986) and Mitchell et al. (2005) reported that the separation position from the coast of the TBTWC path sometimes shifted to lower latitude and the TBTWC disappeared from spring to autumn in 1974, 1981 and 2000. Lee and Niiler (2010a) indicated that the TWC paths do not have seasonal variation and they are classified into three circulation patterns.

As mentioned above, there is not yet consensus on the pattern of the TWC paths. Furthermore, large- and small-scale eddies create large variability in the TWC paths in the southwestern part of the Japan Sea (Katoh, 1993; Isoda and Saitoh, 1993; Morimoto *et al*., 2000), making it difficult to discern the variability in the sea surface current field using ship-observed data. With advances in remote sensing techniques and the expansion of data archives, many useful data have been available for investigation of sea surface variations. In particular, sea surface heights measured by satellite altimeter and sea surface velocity measured by satellite-tracked drifters provide valuable information on sea surface currents.

With use of these two data, we make a long-term dataset of absolute sea surface current (ASSC) and dynamic height (ASSDH) field with high spatial and temporal resolution for the entire Japan Sea and then use the dataset to examine the mean sea surface current paths and seasonal variation in TWC paths in the southwestern part of the Japan Sea (Chapter 2, 3). Moreover, we try to elucidate the variability of the TWC path, especially TBTWC path, by analyzing ASSDH data and to examine which parameters such as wind stress curl, surface cooling, and volume transport of the TWC relates to the interannual variation of the TBTWC path (Chapter 3). In Chapter 4, we try to understand mechanism of TBTWC path variation by mean of a reduced gravity model with simple topography. We summarize in chapter 5 and 6.

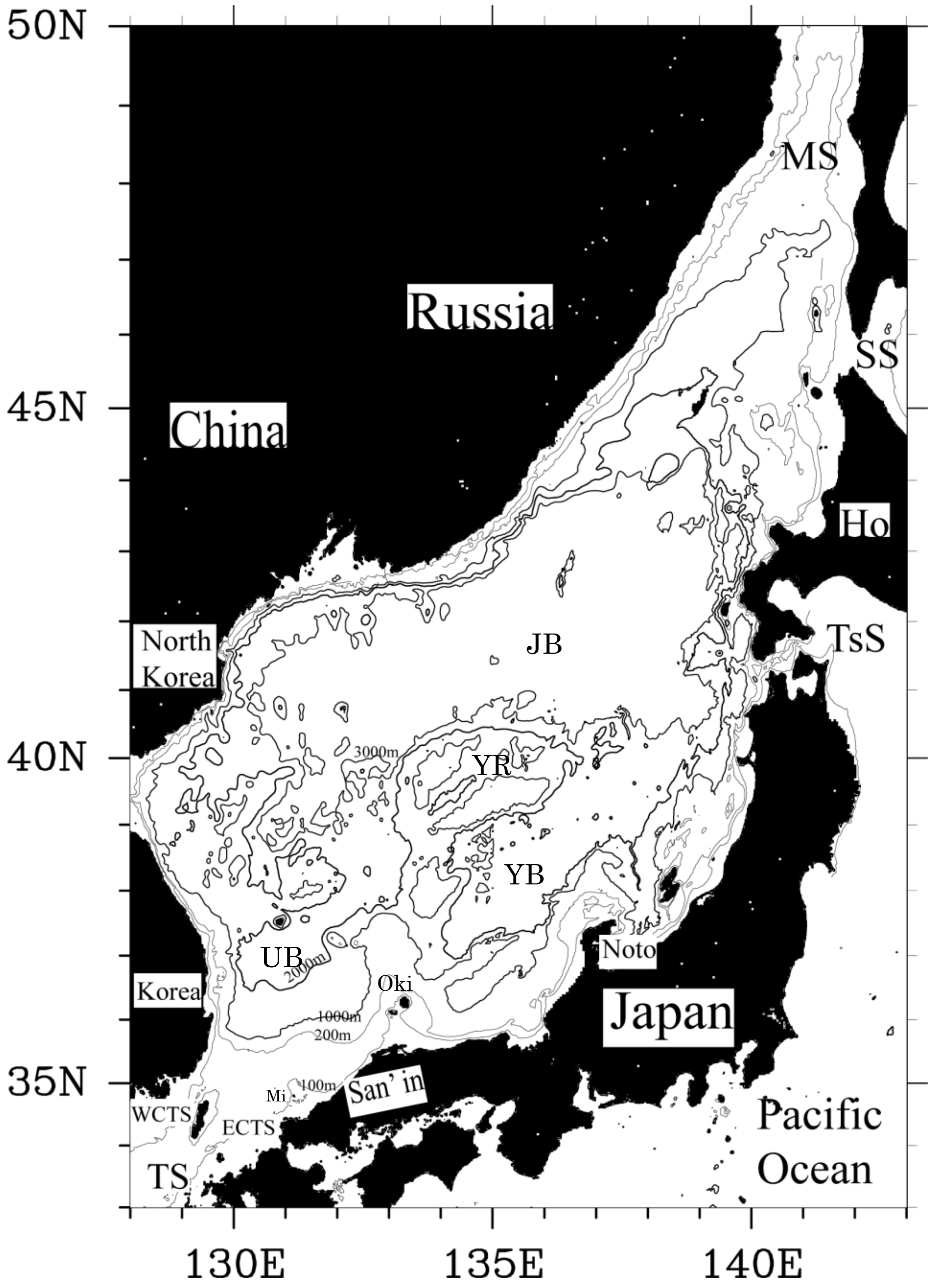

Figure. 1.1: Map and bathymetry of the Japan Sea. TS, ECTS, WCTS, TsS, SS, MS, Noto, Mi, Oki, Ho, JB, YR, UB and YB indicate the Tsushima Strait, the eastern channel of the Tsushima Strait, the western channel of the Tsushima Strait, the Tsugaru Strait, the Soya Strait, the Mamiya (Tatar) Strait, the Noto Peninsula, Mishima Island, Oki Island, Hokkaido, the Japan Basin, the Yamato Rise, the Ulleung Basin, and Yamato Basin, respectively. Numbers show the water depth in meters.

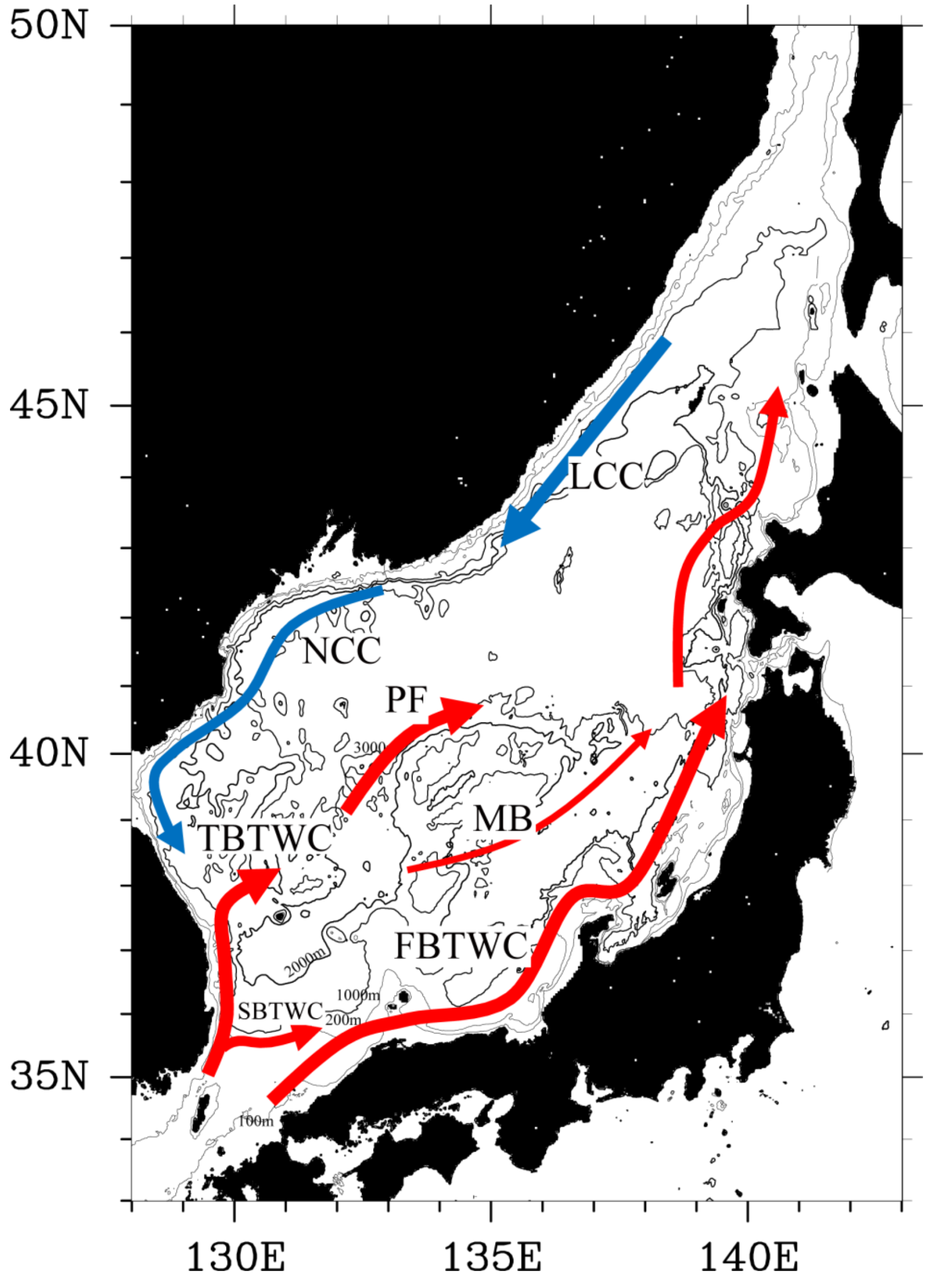

Figure 1.2: Schematic map of sea surface currents. The FBTWC, SBTWC, TBTWC, PF, MB, LCC, and NCC stand for the first branch of the Tsushima Warm Current, the second branch of the Tsushima Warm Current, the third branch of the Tsushima Warm Current, Polar Front, Middle branch, Liman Cold Current, and North Korean Cold Current, respectively. Red and blue arrows represent warm and cold currents, respectively (after Kawabe, 1982; Mooers et al., 2006). The triple branch current pattern consists of current paths of FBTWC, SBTWC and TBTWC in the southwestern part of the Japan Sea.

Chapter 2

Tsushima Warm Current paths in the southwestern part of the Japan Sea

2.1 Introduction

As mentioned in Chapter 1, we make a long-term dataset of the absolute sea surface current (ASSC) with high spatial and temporal resolution for the entire Japan Sea. We use the satellite-tracked drifter data and satellite altimetry data. Satellite-tracked drifter data provide the current velocity at approximately 15 m depth below the sea surface. The Lagrangian drifter data can indicate the absolute sea surface current over large areas. On the other hand, satellite altimeters can provide accurate observations of sea surface height anomaly (SSHA) which is anomaly from temporal average over an observation period. Assuming geostrophic balance, the sea surface current anomaly is derived from the SSHA. Combining satellite-tracked drifter data and satellite altimetry data, the ASSC field can be derived (Uchida and Imawaki, 2003; Ambe *et al.*, 2004).

With use of the dataset, we reveal variation in the TWC path in the Japan Sea, especially southwestern part of the Japan Sea where the TWC paths are complicated.

2.2 Data and Methods

The mean sea surface current field cannot be calculated directly from altimetry data because of the large geoid error, which is greater than oceanic variation in time and space (Imawaki *et al.*, 1991). Although the mean sea surface current field can be estimated by dynamic calculation using historical observations of water temperature and salinity, it is difficult to estimate the field for the entire Japan Sea due to shallow water depths near the coasts where the first branch of the TWC (FBTWC) and the second branch of the TWC (SBTWC) occur. Moreover, the mean sea surface current field estimated from ensemble means of satellite-tracked drifter data would have a bias toward true sea surface current field because of irregular sampling in time and space. Hence, we evaluate the less biased mean sea surface current for the Japan Sea using satellite-tracked drifter data and altimetry data based on the method of Uchida and Imawaki (2003) and Ambe *et al*. (2004). The method is straightforward. The absolute sea surface current $V(r,t)$ at position r and time t can be written as follows:

$$V(r,t) = V_m(r) + V_a(r,t), \tag{2-1}$$

where $V_m(r)$ and $V_a(r,t)$ are the mean sea surface current and its anomaly, respectively. We consider only geostrophic current. $V_a(r,t)$ is derived from the SSHA of altimetry data, and V(r,t) is derived from satellite-tracked drifter data at the time when the drifter exists at position r and time t. As a result, $V_m(r)$ is derived at position r where both altimetry data and satellite-tracked drifter data exist. Once $V_m(r)$ is derived at position r, V(r,t) can be derived by adding $V_a(r,t)$ and $V_m(r)$. The following sections explain the method used to obtain $V_a(r,t)$, $V_m(r)$, and V(r,t) in more detail.

2.2.1 Calculation of the sea surface current anomaly from satellite altimetry data

Eddies with horizontal scales of several tens to several hundreds of kilometers are dominant in the Japan Sea (Isoda, 1994; Morimoto *et al.*, 2000). To examine the variability in the current field including these eddies, we use along-track data from four satellite altimeters, TOPEX/POSEIDON, ERS-2, Envisat, and Jason-1 (Fig. 2.1). TOPEX/POSEIDON and Jason-1 observed sea surface height every approximately 10 days along 13 subsatellite tracks over the Japan Sea. ERS-2 and Envisat observed sea surface height every 35 days along 41 subsatellite tracks. Neighboring satellite tracks of TOPEX/POSEIDON or Jason-1 are approximately 230 km apart, whereas adjacent subsatellite tracks of ERS-2 or Envisat are 60 km apart. We use these altimetry data at the same time to capture the variability in eddies in the Japan Sea.

The altimetry data used here were the Corrected Sea Surface Height data of the

AVISO Delayed Time products. These data were corrected for the effects of wet troposphere, dry troposphere, ionosphere, and electromagnetic bias (AVISO, 2008). Tidal contamination was eliminated using the GOT2000 tide model. Although the tidal model was found to have large error in marginal seas, error was small in the Japan Sea (Morimoto, 2009). ERS-2 and Envisat have the same orbits and TOPEX/POSEIDON and Jason-1 have the same orbits. Biases were found in the Corrected Sea Surface Height data between ERS-2 and Envisat and between TOPEX/POSEIDON and Jason-1. We calculated the average bias between ERS-2 and Envisat as 0.404 m and that between TOPEX/POSEIDON and Jason-1 as 0.098 m. We connected the data for each satellite after eliminating the average bias. There was no bias between ERS-2 and TOPEX/POSEIDON after the AVISO correction.

The SSHAs at the observation points along subsatellite tracks are anomalies from the temporally averaged sea surface heights over the observed period (13 years and 8 months from May 1995 to January 2009). To obtain the distribution of monthly mean SSHA, the SSHAs were interpolated to every 0.25°×0.25° grid point by the optimal interpolation method (Imawaki *et al.*, 1991). The covariance functions of signal and noise must be decided in advance for the optimal interpolation method. The following equations are the applied covariance functions for signal W(|R|) and noise σ_e, respectively:

$$W(|R|) = w_0^2 \exp\left\{-\left(\frac{|R|}{L}\right)^2\right\}, \tag{2-2}$$

$$\sigma_e = \sigma\delta(\Delta t), \tag{2-3}$$

where $\delta(\Delta t)$ is 1.0 at $\Delta t = 0$ and 0.0 at $\Delta t \neq 0$, |R| denotes the distance between a grid center and the position of the SSHA data, L is the de-correlation scale, w_0 is the magnitude of the signal (L = 80 km, w_0 = 5.4 cm); and σ (= 7.8 cm) denotes the magnitude of noise. The magnitudes of w_0 and σ were decided using the autocorrelation function. Assuming geostrophic balance, we calculated the sea surface current anomalies $V_a(r,t)$ in equation (2-1) during the 13 years and 8 months from the monthly SSHA field.

2.2.2 Calculation of the mean sea surface current and absolute sea surface current

Satellite-tracked drifter data have been collected by the World Ocean Circulation Experiment (WOCE)-Tropical Ocean and Global Atmosphere (TOGA) Surface Velocity Program (SVP) (WOCE/SVP). The WOCE/SVP drifters have a holey-sock type drogue centered at a depth of 15 m. A number of WOCE/SVP drifters were released along the east coast of Korea or the southern coast of Russia (Fig. 2 of Watanabe *et al.*, 2009). Therefore, the densities of the satellite-tracked drifter data around Japanese coast were relatively low.

To increase the satellite-tracked drifter data around the Japanese coast, we used 77 satellite-tracked drifters (ZTB-R1S4; Zeni Lite Buoy Co., Ltd) released by the Japan Sea National Fisheries Research Institute of the Fisheries Research Agency (JSNFRI) from June 2004 to September 2008. Our drifters are 0.34 m in diameter, 0.3 m in height, and 6.5 kg in weight. In total, 157537 satellite-tracked drifter data every 6 hours were available in the entire Japan Sea from May 1995 to January 2009 (Fig. 2.1). The WOCE/SVP and JSNFRI drifter data were interpolated at 6 hours intervals using the method of Hansen and Poulain (1996).

Because we need the geostrophic component in the satellite-tracked drifter data, ageostrophic components such as tidal current, inertial oscillation, and wind-driven current must be eliminated. First of all, since the satellite-tracked drifter data were adjusted to the horizontal scale of satellite altimetry data of about 60 km, we applied 78 hours running mean based on an average speed of TWC of 20 cm s^{-1} (Katoh, 1993; Morimoto and Yanagi, 2001). Tidal current and inertial oscillation were also removed by this processing. Then we eliminated wind-driven currents which are evaluated from wind data using a wind magnitude factor and an angle relative to wind direction. To derive the wind magnitude factor and the angle, wind data at 10 m above the sea surface every 6 hours from the Japanese 25-year Reanalysis product (Onogi *et al.* 2007) and $V_a(r,t)$ in equation (2-1) were used. The wind data were recalculated by the 78 hours running mean so that the wind and satellite-tracked drifter data would have the same timescale.

We interpolated the wind and satellite-tracked drifter data to each SSHA grid point r and time t (center day of month) by the following functions:

$$V_{buoy}(r,t) = \frac{\sum_{i=1}^{N} W_i(r_i,t_i)V_{ib}(r_i,t_i)}{\sum_{i=1}^{N} W_i(r_i,t_i)}, \tag{2-4}$$

$$W_i(r_i,t_i) = \exp\left\{-\frac{(r-r_i)^2}{L_r^2} - \frac{(t-t_i)^2}{L_t^2}\right\}, \tag{2-5}$$

where $V_{buoy}(r,t)$ indicates the interpolated velocity of satellite-tracked drifter data at position r and time t, $V_{ib}(r_i,t_i)$ is the velocity of a satellite-tracked drifter, $W_i(r_i,t_i)$ is a weight function, L_r is 25 km, and L_t is 10 days. Wind data were interpolated in the same manner as the satellite-tracked drifter data using the following functions:

$$V_{wind}(r,t) = \frac{\sum_{i=1}^{N} W_{iwind}(r_i)V_{wind}(r_i,t)}{\sum_{i=1}^{N} W_{iwind}(r_i)}, \tag{2-6}$$

$$W_{iwind}(r_i) = \exp\left\{-\frac{(r-r_i)^2}{L_{wr}^2}\right\}, \tag{2-7}$$

where $V_{wind}(r,t)$ indicates interpolated wind data, $W_{iwind}(r_i)$ is a weight function, and L_{wr} equals 100 km.

A flow in the grid, $V_{buoy}(r,t)$ of equation (2-4), is separated as follows (Centurioni *et al.*, 2009):

$$V_{buoy}(r,t) = V_{mg}(r) + V_a(r,t) + V_w(r,t), \tag{2-8}$$

where all terms are complex numbers. The real and imaginary part correspond to the x and y components, respectively. The $V_{mg}(r)$ and $V_a(r,t)$ denote the time-averaged sea surface current and its anomaly which was derived at section 2.2.1, respectively, and $V_w(r,t)$ represents the wind-driven current and is written by the following equation:

$$V_w(r,t) = \mathbf{A} \mid V_{wind}(r,t)|\exp\{\boldsymbol{i}(\theta - \psi)\}, \tag{2-9}$$

here, $\boldsymbol{i}$ is the imaginary unit, **A** is the wind magnitude factor (which is a coefficient of the changing magnitude of wind velocity), θ is the angle of wind relative to east (positive in the anticlockwise direction), and ψ is the angle relative to the downstream wind direction (positive in the clockwise direction). The equation (2-9) is decomposed as follows,

$$V_w(r,t) = [X_1|V_{wind}(r,t)|\cos\theta + X_2|V_{wind}(r,t)|\sin\theta] + \boldsymbol{i}[X_3|V_{wind}(r,t)|\sin\theta - X_4|V_{wind}(r,t)|\cos\theta],$$

where X_1, X_3 and X_2, X_4 denote $\mathbf{A}\cos(\psi)$ and $\mathbf{A}\sin(\psi)$, respectively. We have already obtained $V_{buoy}(r,t)$, $V_a(r,t)$, $V_{wind}(r,t)$, and θ in equation (2-8) at the grid point over time and space during May 1995 through January 2009. Therefore, unknown terms $V_{mg}(r)$, X_1, X_2, X_3, and X_4 are calculated by minimizing the following cost functions Y_x for x component, and Y_y for y component:

$$Y_x=[\mathrm{Re}\{V_{buoy}(r,t) - V_{mg}(r) - V_a(r,t)\} - X_1|V_{wind}(r,t)|\cos\theta - X_2|V_{wind}(r,t)|\sin\theta]^2, \quad (2\text{-}10)$$

$$Y_y=[\mathrm{Im}\{V_{buoy}(r,t) - V_{mg}(r) - V_a(r,t)\} - X_3|V_{wind}(r,t)|\sin\theta + X_4|V_{wind}(r,t)|\cos\theta]^2. \quad (2\text{-}11)$$

We calculate $\frac{\partial \sum Y_x}{\partial V_{mg}(r)} = 0$, $\frac{\partial \sum Y_x}{\partial X_1} = 0$, and $\frac{\partial \sum Y_x}{\partial X_2} = 0$ for equation (2-10), and $\frac{\partial \sum Y_y}{\partial V_{mg}(r)} = 0$, $\frac{\partial \sum Y_y}{\partial X_3} = 0$, and $\frac{\partial \sum Y_y}{\partial X_4} = 0$ for equation (2-11) by the least-squares method. We can obtain two approximately equal values of **A** from both the x component ($= \sqrt{X_1^2 + X_2^2}$) and y component ($= \sqrt{X_3^2 + X_4^2}$), and ψ from both the x component ($= \tan^{-1}\left(\frac{X_2}{X_1}\right)$) and y component ($= \tan^{-1}\left(\frac{X_4}{X_3}\right)$). Therefore, we obtained values of **A** and ψ respectively of 0.008 and 58.2° by averaging these values for the x and y component over the entire Japan Sea.

The geostrophic component of satellite-tracked drifter data was derived by eliminating wind-driven current using A and ψ. The processed satellite-tracked drifter data were interpolated into each SSHA grid point by equation (2-4). If both the processed satellite-tracked drifter and the sea surface current anomaly data numbered more than five in a grid point (Fig. 2.2), the mean sea surface current, $V_m(r)$, was calculated for that location. Then we obtained the mean sea surface current field for the entire Japan Sea as shown in Fig. 2.3. We calculated monthly absolute sea surface current shown as V(r,t) in equation (2-1) by adding the sea surface current anomaly derived from the SSHA and the mean sea surface current.

2.2.3 Validation of absolute sea surface current data

At first, we examine the stability of the mean sea surface current speed and direction relative to the averaged data number for estimating mean sea surface current. Here we define the spatial average of RMS difference ΔA_n^m between a mean sea surface current $V_m(r_j)$ for an average number of m shown in Fig. 2.2 and a sea surface current $V_n(r_j)$ for average number of n $(2 \le n \le m)$ at the grid point j.

$$\Delta A_n^m = \frac{\sum_{j=1}^{jn} \sqrt{(V_m(r_j))^2 + (V_n(r_j))^2 - 2|V_m(r_j)||V_n(r_j)|\cos\theta_j}}{|V_m(r_j)|} . \quad (2\text{-}12)$$

Here the jn is the number of the grid point for the average number of m, and the θ_j is the difference in current direction between $V_m(r_j)$ and $V_n(r_j)$. We selected m=32 because of the large values of both m and jn. The slope of the line seems to change at n=5 (Fig. 2.4a). It is supposed that the number n=5 might be the starting point of stable to estimation of the mean sea surface current. When n is more than 10, ΔA_n^m is less than 0.4. Hence, the mean sea surface current value might be nearly independent of the averaged data number.

Next, to verify the accuracy of the absolute sea surface currents V(r,t), we compared the absolute sea surface currents V(r,t) in equation (2-1) and the absolute sea surface currents $V_{drifter}$(r,t) derived from satellite-tracked drifters (Fig. 2.4b). The V(r,t) were derived by adding the mean sea surface current shown in Fig. 2.3 to the sea surface current anomalies calculated from altimetry data from June to August 2010. Note that the absolute sea surface current V(r,t) were derived for 7.5 days interval. The $V_{drifter}$(r,t) were calculated data obtained from five satellite-tracked drifter's data during June to August 2010 by the same manner in section 2.2.2. The data from these drifters were not used when the mean sea surface current shown in Fig. 2.3 was calculated. Namely, the sea surface currents observed by these five drifters are independent of V(r,t). We could get 53 matched data points between V(r,t) and $V_{drifter}$(r,t) from June to August 2010. In Fig. 2.4b, the x axis indicates the ratio of current speed of V(r,t) to $V_{drifter}$(r,t), and the y axis indicates the difference of current direction between V(r,t) and $V_{drifter}$(r,t). The square, circle, star, and cross indicate the averaged number to estimate mean sea surface current at each grid point. The ratios of current speed were between 0.4 and 1.2. This result indicates that the current speed of the absolute sea surface current V(r,t) is slightly smaller than the satellite-tracked drifter data $V_{drifter}$(r,t) because of smoothing by the interpolation procedure. The data relative to the difference in current directions were plotted between about 30° to -40°. In addition, 89% of the data were plotted between 20° and -20°, and 60% of the data were between 10° and -10°. The data averaged less than 5 has a tendency of large error shown by signs of cross. On the other hand, the data averaged more than 5 which are shown by square, circle, and star range from about 30° to -30°. Therefore, we consider that the mean sea surface current derived from the data number more than 5 and our dataset of absolute sea surface currents V(r,t) are sufficient for identifying current paths in the Japan Sea.

2.3 Results

2.3.1 Mean sea surface current field of the TWC

Figure 2.3 shows the mean sea surface current field. There are two strong currents in the Tsushima Strait. One flows along the Japanese archipelago through the eastern channel of the Tsushima Strait and reaches the Tsugaru Strait; this is the FBTWC. The other flows northward along the east coast of the Korean Peninsula to 38°N. Then, it turns to the east and separates into two current paths around 38°N, 131°E. One of these currents flows northeastward, and around 39.5°N, 131°E it joins the eastward flow that originated at 39°N, 128.5°E. The other current flows southeastward, meanders and joins the strong northward flow around north of Oki Island. Then the confluent current flows eastward as strong currents, eventually reaching the Tsugaru Strait. In the northern part of the Japan Sea, a relatively strong northward current can be seen west of Hokkaido.

In the southwestern part of the Japan Sea, from 33–40°N, 127–134°E, the mean sea surface current shows the triple-branch pattern proposed by previous studies (Kawabe 1982a, b; Katoh, 1994b; Hase *et al.*, 1999). In addition to the FBTWC and the third branch of the TWC (TBTWC), the SBTWC flows eastward around 35.5°N, 131°E. The average current velocities of the FBTWC, SBTWC, and TBTWC are 20, 12, and 25 cm s^{-1} in the regions of 34–35°N, 130–131°E; 35.25–35.75°N, 130.5–131°E; and 35.5–37°N, 129.5–130.25°E, respectively. Near the coast around 35–36°N, 131–133°E, the FBTWC and SBTWC are not separated.

2.3.2 Seasonal variation in the triple branches of the TWC in the southwestern part of the Japan Sea

2.3.2.1 Method of analysis for seasonal variation in current paths

We examine the seasonal variation in the sea surface currents using frequency analysis and the standard deviation of sea surface currents normalized by monthly mean in each month. Figure 2.5 shows the procedure for frequency analysis. Figure 2.5a denotes a monthly mean sea surface current velocity in a grid. We divide the data into to four quadrants relative to the monthly mean current and counted the number of current in each range using the approximately 13 years of data (Fig. 2.5b). By this method, we obtained the frequency of current direction. Figure 2.6 shows the frequency of current direction and normalized standard deviation with monthly mean current velocity in the southwestern part of the Japan Sea for each month. The frequency of current direction is shown by line color, with red, blue, and black lines indicating frequencies greater than 70%, greater than 50% but less than 70%, and less than 50%, respectively. The normalized standard deviation is shown by color shading with monthly mean sea surface current velocity. For the normalized standard deviation, warmer colors indicate that the current speed variability is greater than the monthly mean sea surface current; that is, the current speed is variable in those areas. In contrast, cooler colors indicate that the current speed is almost the same magnitude as the monthly mean sea surface current; that is, current speed is stable at these grid points.

We define current paths as “highly stable,” “stable,” “unstable,” and “highly unstable” based on the frequency analysis and normalized standard deviation as follows. Red lines and blue shading indicate “highly stable,” red and blue lines and green shading indicate “stable,” blue lines and yellow shading indicate “unstable,” and no line and red shading indicate “highly unstable.” For instance, the area around the east coast of the Korean Peninsula around 35–38°N, 130°E has red lines and blue shading in January (Fig. 2.6). This suggests that current direction was stable and current speed was almost the same magnitude as the monthly mean sea surface current. That is, the current path in this area was highly stable.

2.3.2.2 Seasonal variation in TWC paths

The FBTWC area along the coast of Japan had red lines and blue shading in all months from the eastern channel of the Tsushima Strait to west of Oki Island. This result places the FBTWC in the highly stable category. Our result is similar to previous findings (Katoh, 1993, 1994a, b; Hase *et al*., 1999). Over the continental shelf around 35–36°N, 131–133°E, a wide stable current path (red lines and blue shading) exists throughout the year. In this area, the FBTWC and SBTWC seem to be joined.

The TBTWC along the east coast of the Korean Peninsula has red lines up to 38°N in all months except October. In October, there are red lines to 39°N and then blue and green shading around 39°N. In this area, the current path is highly stable up to 38°N and stable from 38–39°N. At 38°N, 130–131°E the TBTWC separates into two directions with a stable current from June to February except in January. A current that separates from the TBTWC at 38°N, 131°E continues southeastward and then merges with a northward current west of Oki Island in June, September, and December. The current path is stable during these months. The other current path continues northeastward and joins the eastward current that originated at 39°N, 128.5°E from June to February, except in January. This current path area has red and blue lines and green shading, and thus is considered stable.

The northward current west of Oki Island continues up to 38.5°N as a highly stable current throughout the year except from March to July. From March to July, the current is stable. Around 39.5°N, 129°E, there is stable clockwise circulation in all months. In particular, the circulation in November and December is clearer and more stable than in other months. Along 39.5°N, 128.5–131°E, there is a stable eastward current with small meanders in all months. From 39.5°N, 131–132°E, the current path is unstable or highly unstable from December through April. In contrast, the current path is stable from May through November.

The SBTWC path is shown in Fig. 2.7, which is the same as Fig. 2.6 but enlarged around the continental shelf edge at 34.5–36.5°N, 129–132°E. The SBTWC flows along the continental shelf edge at the 200-m isobath in all months. The current speed reaches a maximum in August and minimum in November around the continental shelf edge (Fig. 2.8). The line/shading results show that the SBTWC is a stable current except in

November.

2.3.2.3 FBTWC and SBTWC paths at the continental shelf

Near the coast around 35–36°N, 131–133°E, the FBTWC and SBTWC are not separated in our grid data (Figs. 2.6 and 2.7). However, previous research has suggested that the FBTWC and SBTWC separate into branches in this region (Morimoto *et al*., 2009a). To investigate the FBTWC and SBTWC in this area, the absolute sea surface current perpendicular to the subsatellite track was calculated at each altimetry observation point. The currents were derived every 7 km and approximately 10 days by the same method as described in section 2 with a de-correlation scale of space L_r (21 km) and time L_t (10 days).

Figure 2.9 shows the frequency of current direction and the normalized standard deviation. The line and arrow types in Fig. 2.9 correspond to the line and shading colors in Fig. 2.6, respectively. The left panel shows the frequency of current direction in each month and the right panel shows the monthly mean current velocity perpendicular to the subsatellite track with standard deviation normalized by the monthly mean current speed.

There are two modes in each month where the normalized standard deviation is less than 2 (solid arrows); these modes are denoted by open circles (Fig. 2.9). Here, the offshore and nearshore modes are regarded as the offshore and nearshore current paths, respectively. The mean current speeds of the nearshore and offshore currents are 23 cm s^{-1} and 19 cm s^{-1}, respectively. These current paths are highly stable throughout the year.

2.4. Discussion

Nearshore and offshore current paths occurred throughout the year as highly stable currents in the continental shelf east of 131°E (Fig. 2.9). The FBTWC continues in a nearshore path and the SBTWC seems to continue in an offshore path. However, although the SBTWC was unstable in November (Fig. 2.7), the offshore current path was a highly stable current (Fig. 2.9). Katoh (1994b) reported from acoustic Doppler current profiler data that the FBTWC bifurcated north of Mishima Island in summer. In addition, Hirose *et al*. (2009) suggested that there were two current paths downstream of Mishima Island. Moreover, southward flow over the continental shelf originating from the TBTWC was suggested in Fig. 4 of Watts *et al*. (2006). The frequency of current direction in Fig. 2.6 also shows southward flow from the TBTCW, especially in April. These previous studies and our results imply that an offshore current path originates from the SBTWC, that the FBTWC might bifurcate after passing by the north side of

Mishima Island, and that southward flow may emerge north of the continental shelf edge.

The offshore current generally corresponds to a large water temperature gradient at 100 m depth (Fig. 2.10). Hase *et al*. (1999) previously noted this relation, and Kawabe (1982b) reported that the SBTWC is caused by the lowest two modes of upper shelf waves at the shelf edge when the volume transport through the western channel of the Tsushima Strait increases. To examine the relationship between volume transport and formation of the SBTWC, correlation coefficients were calculated between sea surface current velocity perpendicular to the subsatellite tracks along pass 112 and pass 750 (Fig. 2.11a) and volume transport through the western channel of the Tsushima Strait estimated by the method of Takikawa and Yoon (2005) (Fig. 2.11b). Along pass 750, correlation coefficients were greater than 0.5 in February and March and greater than 0.4 in June to October around the continental shelf edge. In these periods, volume transport through the western channel of the Tsushima Strait was increased. These results correspond to the generation mechanism of the SBTWC explained by Kawabe (1982b). On the other hand, in pass 112, the correlation coefficient was less than 0.3 around the continental shelf edge. There was less relation to the variability in volume transport in the western channel of the Tsushima Strait. This region has complicated flow and may be the joining region of the FBTWC, SBTWC, and southward flow from the north. Moreover, bottom cold water exists at the continental shelf shallower than 200 m depth (Ogawa and Moriwaki, 1986; Moriwaki and Ogawa, 1988, 1989). Yamazaki (1969) reported that this bottom cold water appeared on a seasonal timescale and for several months. The existence of such water suggests the possible existence of a baroclinic current (Isoda and Murayama, 1990). Therefore, the correlation between the current perpendicular to pass 112 and volume transport in the western channel of the Tsushima Strait might be small.

The TBTWC was stable around 38–39°N east of the Korean Peninsula. Downstream of this region, it split into two stable currents. Previous studies have reported one current path with no split (Tanioka, 1968; Lee and Niiler, 2010a, b). However, our result showed two current paths (southeastward and northeastward currents) from June to February except in January. Especially in June, September, and December, these two current paths joined with another current with a stable path. These current paths are influenced by eddies such as the Ulleung warm eddy and the Takeshima cold eddy (referred to as the Dok Cold Eddy by Mitchell *et al*., 2005). Thus, the positions of eddies are important to the current path pattern in the southwestern part of the Japan Sea.

Our results indicated seasonal variation in the eastward current path around 39.5°N, 128.5–132°E. This current path with small meanders existed in all months and was stable up to around 39.5°N, 131°E except in May through November, during which it remained stable to around 39.5°N, 132°E.

Around 39.5°N, 129°E, a stable current path with a clockwise direction was indicated. This result is almost the same as that shown in Fig. 4 of Watanabe *et al*. (2009) and Fig. 2.6 of Mooers *et al*. (2006) and as reported by Lee and Niiler (2005). On the other hand, Lee and Niiler (2010b) showed a different pattern of anticlockwise current. Like the present study, Lee and Niiler (2010b) used satellite altimetry and satellite-tracked drifter data. Nevertheless, the opposite result was derived. This might be because Lee and Niiler (2010b) used grid altimetry data provided from AVISO, which can be contaminated by large error near the coast.

Northward flow west of Oki Island corresponds to the Japan Sea Current in Fig. 16 of Lee and Niiler (2005) (who called this the East Sea Current). Our results newly indicate seasonal variation in this current path.

2.5. Summary

Our results provide a schematic view of the paths of the TWC in the southwestern part of the Japan Sea (Fig. 2.12). The FBTWC through the eastern channel of the Tsushima Strait flows along the Japanese archipelago in all months as a highly stable current. The TBTWC through the western channel of the Tsushima Strait flows along the east coast of the Korean Peninsula in all months and is also classified as highly stable. Two current paths separate from the TBTWC around 38°N, 130°E. The southeastward current is stable in June, September, and December. The northeastward current is also stable from June to February except in January. The SBTWC west of 131°E flows as a stable current throughout the year except in November. East of 131°E, the offshore current path appears as a highly stable current in all months. This current path originates from the SBTWC, and the FBTWC might bifurcate after passing north of Mishima Island, and then southward flow may arise in the north. The nearshore current path originates from the FBTWC. The northward current west of Oki Island flows as a highly stable current throughout the year except in March to July with stable flow up to around 38.5°N. The eastward current originates around 39°N, 128.5°E and has stable flow around 39.5°N, 128.5–131°E in all months except May to November. In May through November, this current is stable up to 39.5°N, 132°E.

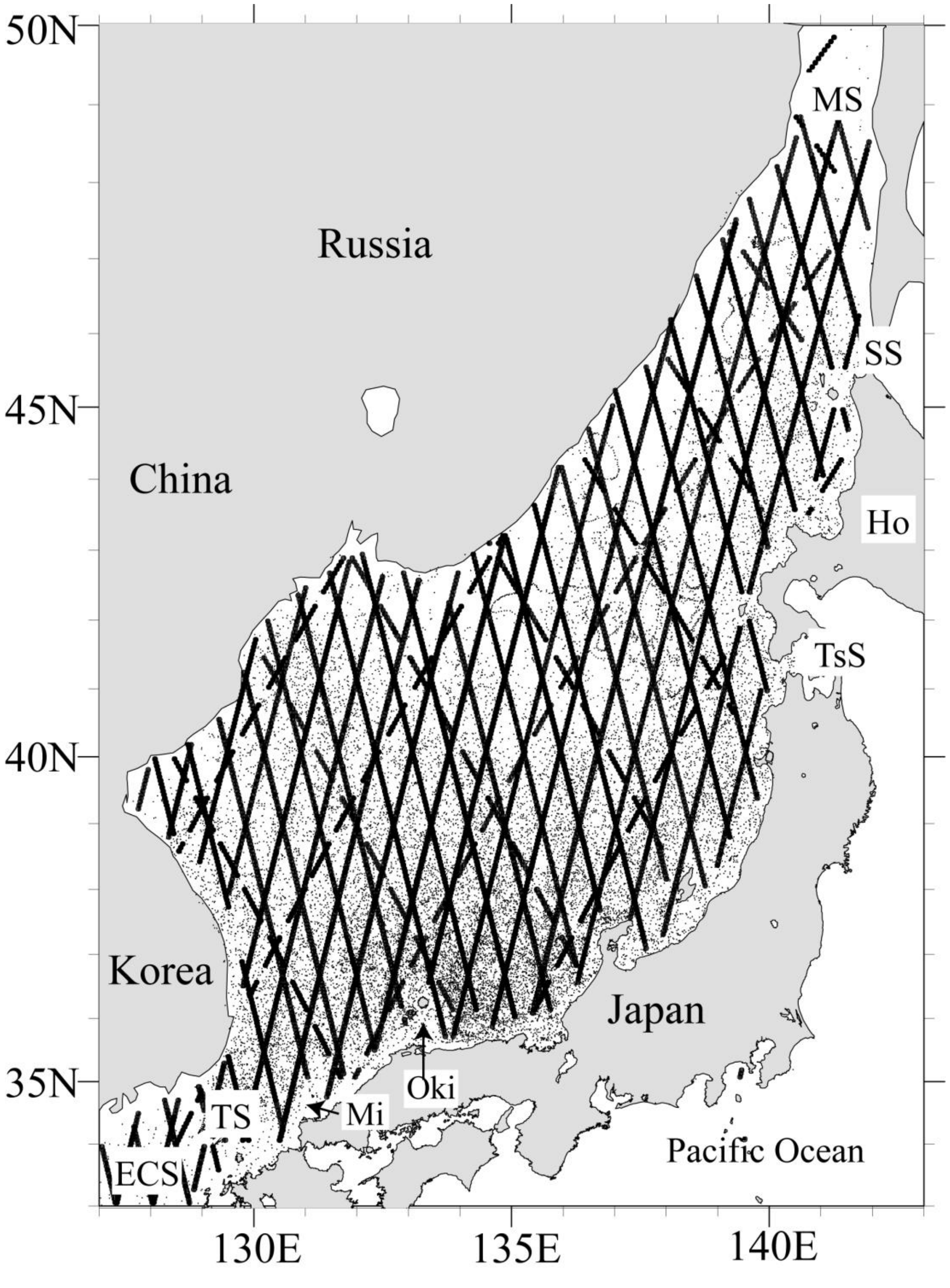

Figure 2.1: Map of the Japan Sea. Satellite tracks of TOPEX/POSEIDON and Jason-1 (broken lines), ERS-2 and Envisat (solid lines), and satellite-tracked drifter data points during May 1995 through January 2009(dots). Mi, TS, and ECS indicate Mishima Island, Tsushima Strait, and East China Sea.

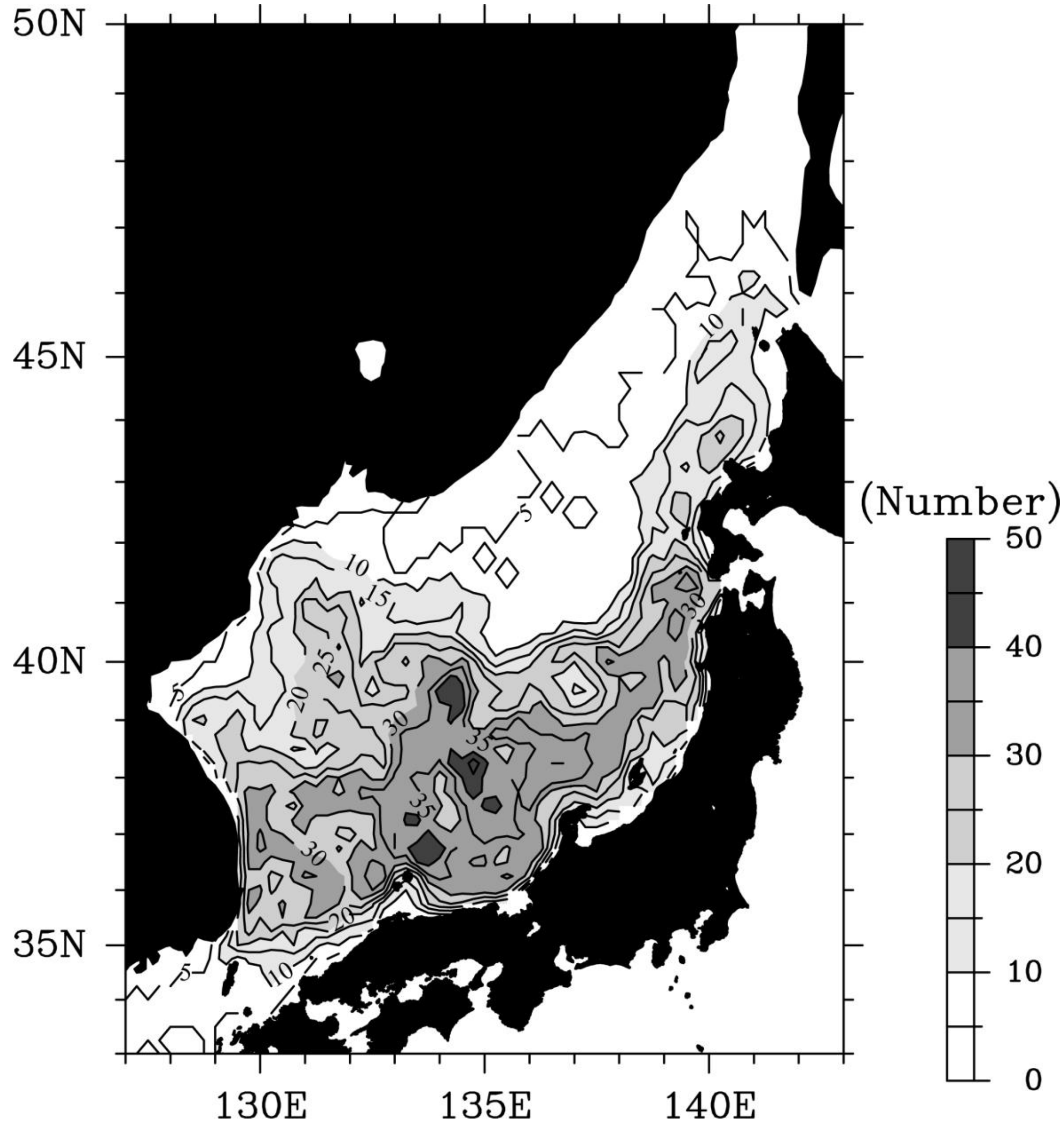

Figure 2.2: The number of data used to estimate mean sea surface current during May 1995 through January 2009 at the grid point. Monochrome shading and contour indicate the number of data.

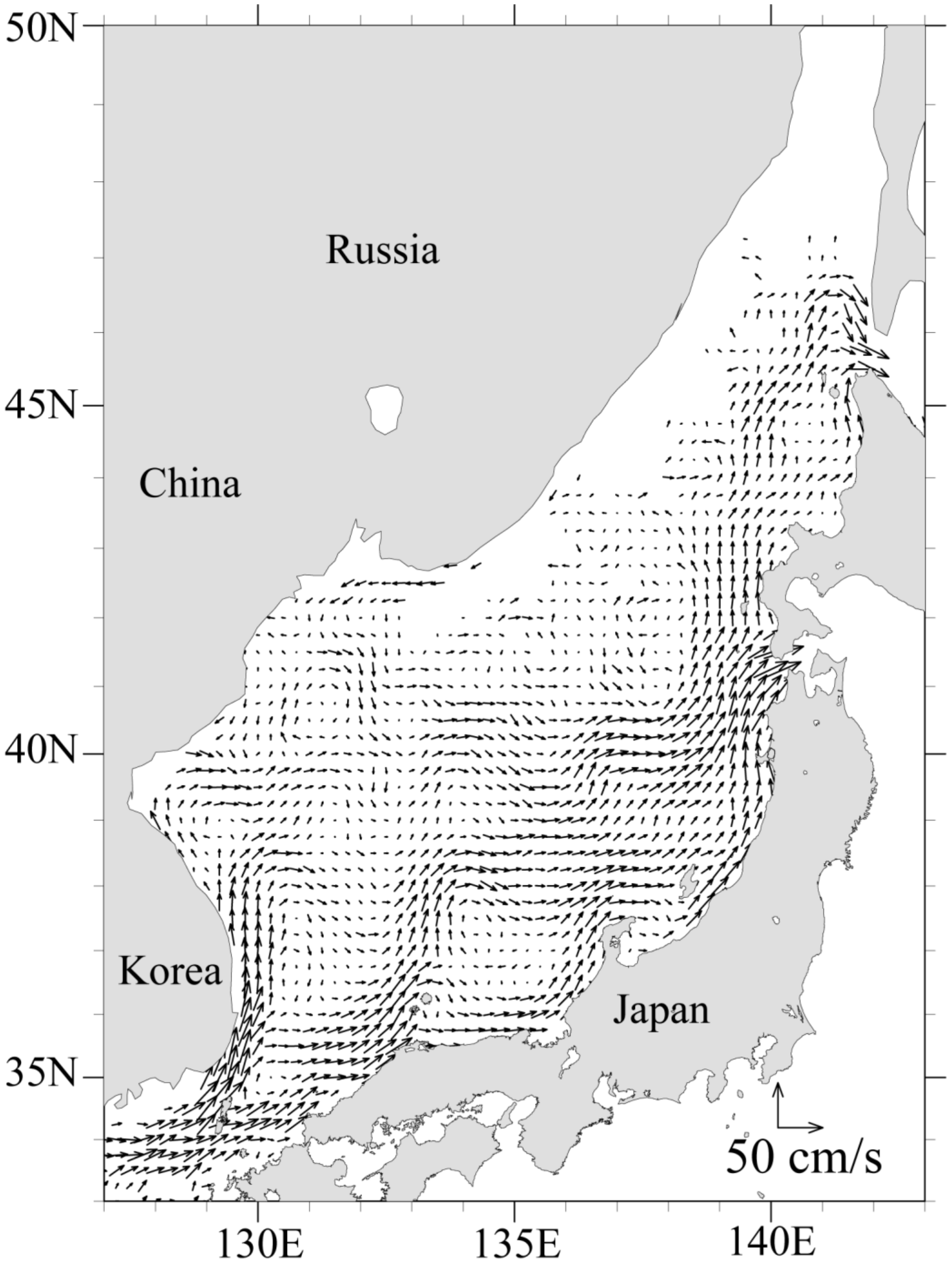

Figure 2.3: Mean sea surface current field in the Japan Sea during May 1995 through January 2009 derived from satellite altimetry and satellite-tracked drifter data.

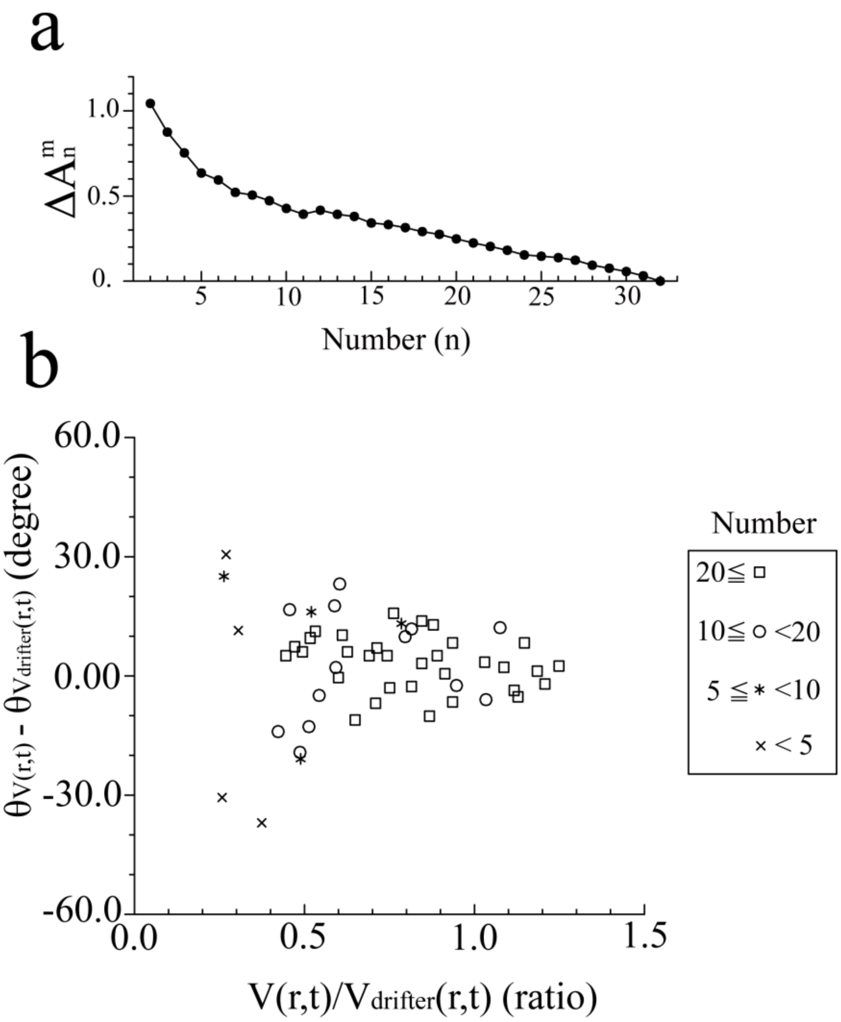

Figure 2.4: (a) Graph for the average number of n relative to the spatial average of RMS difference ΔA_n^m. (b) The graph shows the ratio of sea surface current speed (horizontal axis) vs. difference in current direction (vertical axis) between V(r,t) derived from combining satellite altimetry with satellite-tracked drifter data and $V_{drifter}(r,t)$ derived from only satellite-tracked drifter data. Signs of square, circle, star, and cross indicate the average data number for estimating the mean sea surface current at the grid point. $V(r,t)/V_{drifter}(r,t)$ and $\theta_{V(r,t)} - \theta_{Vdrifter}(r,t)$ indicate the ratio of speed and the difference in current direction, respectively.

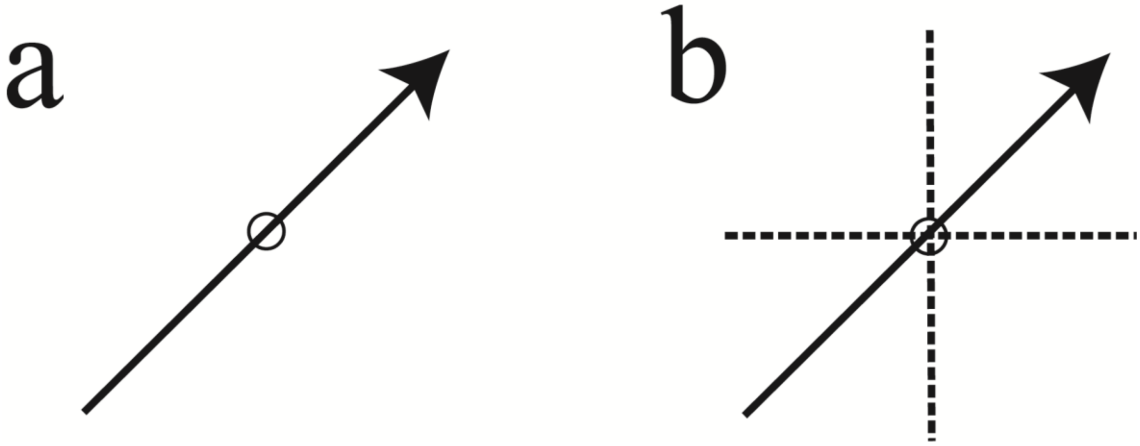

Figure 2.5: Frequency analysis of sea surface current direction. (a) Monthly mean sea surface current at a grid point. A circle indicates a grid point. (b) Four ranges (separated by dotted lines) relative to monthly mean sea surface current.

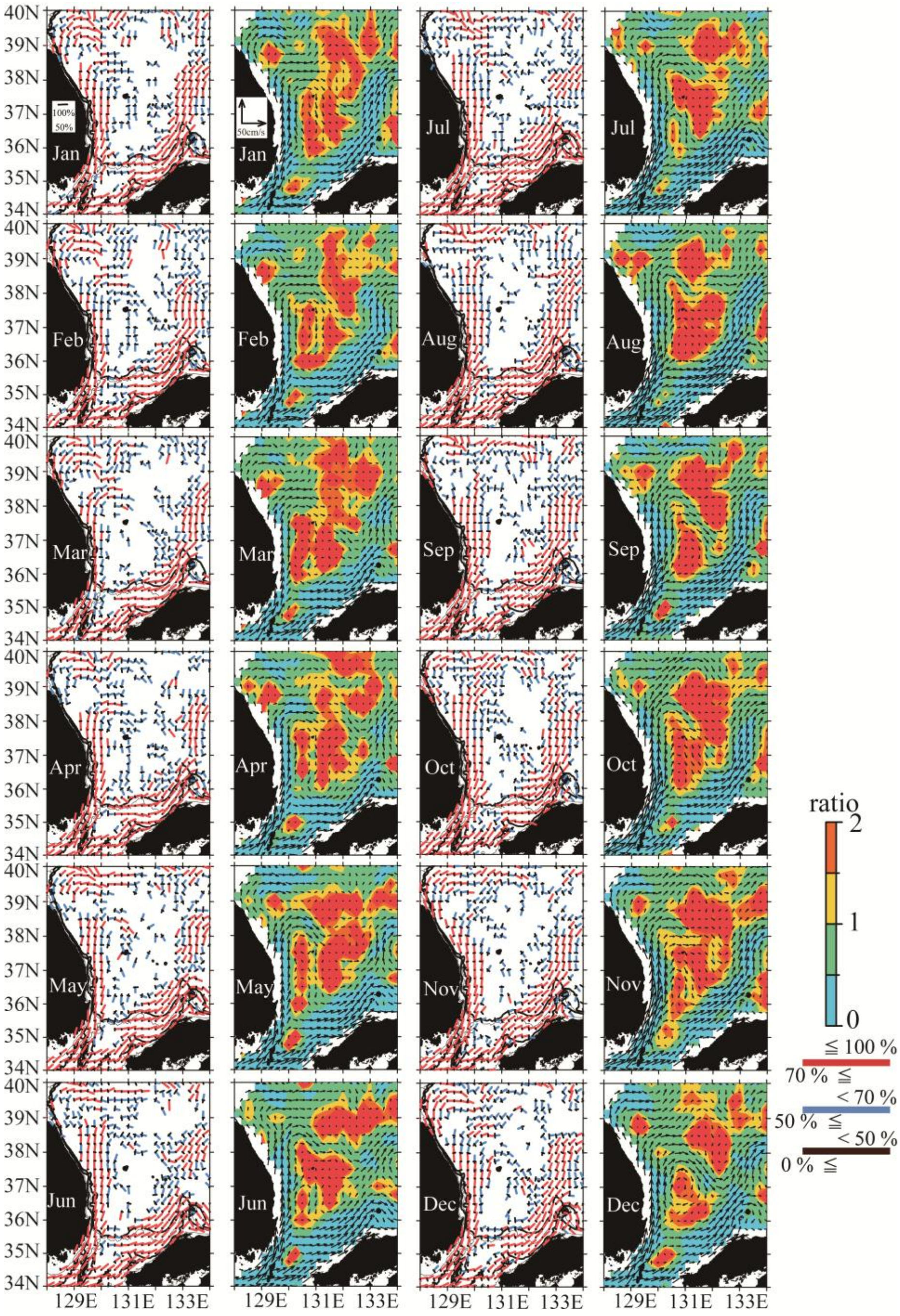

Figure 2.6: Frequency of current direction (left side) and standard deviation normalized by monthly mean sea surface current speed (right side) with monthly mean sea surface current velocity from January to December. The line color and length show the magnitude of frequency for current direction. Red, blue, and black lines indicate frequencies of greater than 70%, greater than 50% but less than 70%, and less than 50%, respectively. No line means that the frequency is less than 50%. The color of shading indicates the standard deviation normalized by the monthly mean sea surface current speed.

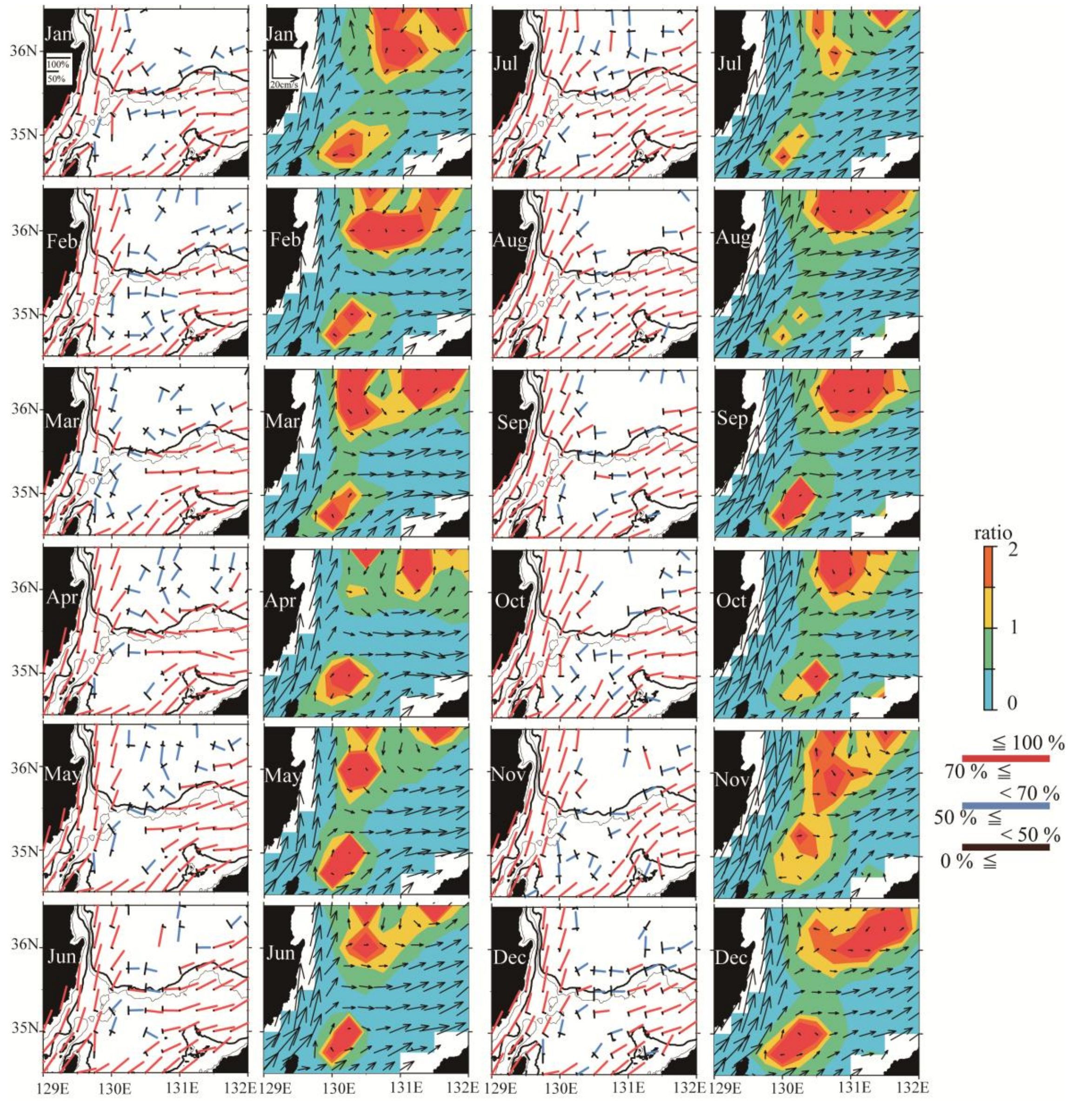

Figure 2.7: Same as Fig 2.6 but enlarged around the continental shelf edge (34.5–36.5˚N, 129–132˚E).

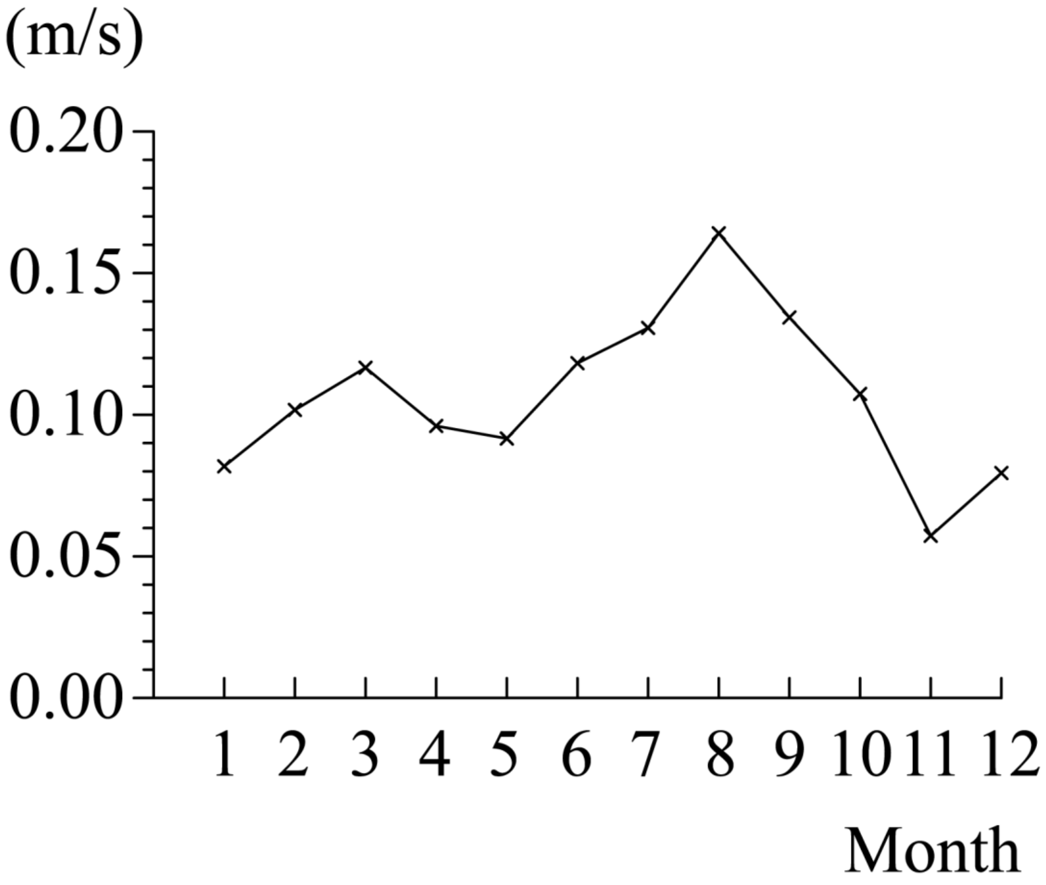

Figure 2.8: Time series of monthly mean current velocity around the continental shelf edge in the region 35.25–35.75˚N, 130.25–130.75˚E. Positive values indicate eastward flow.

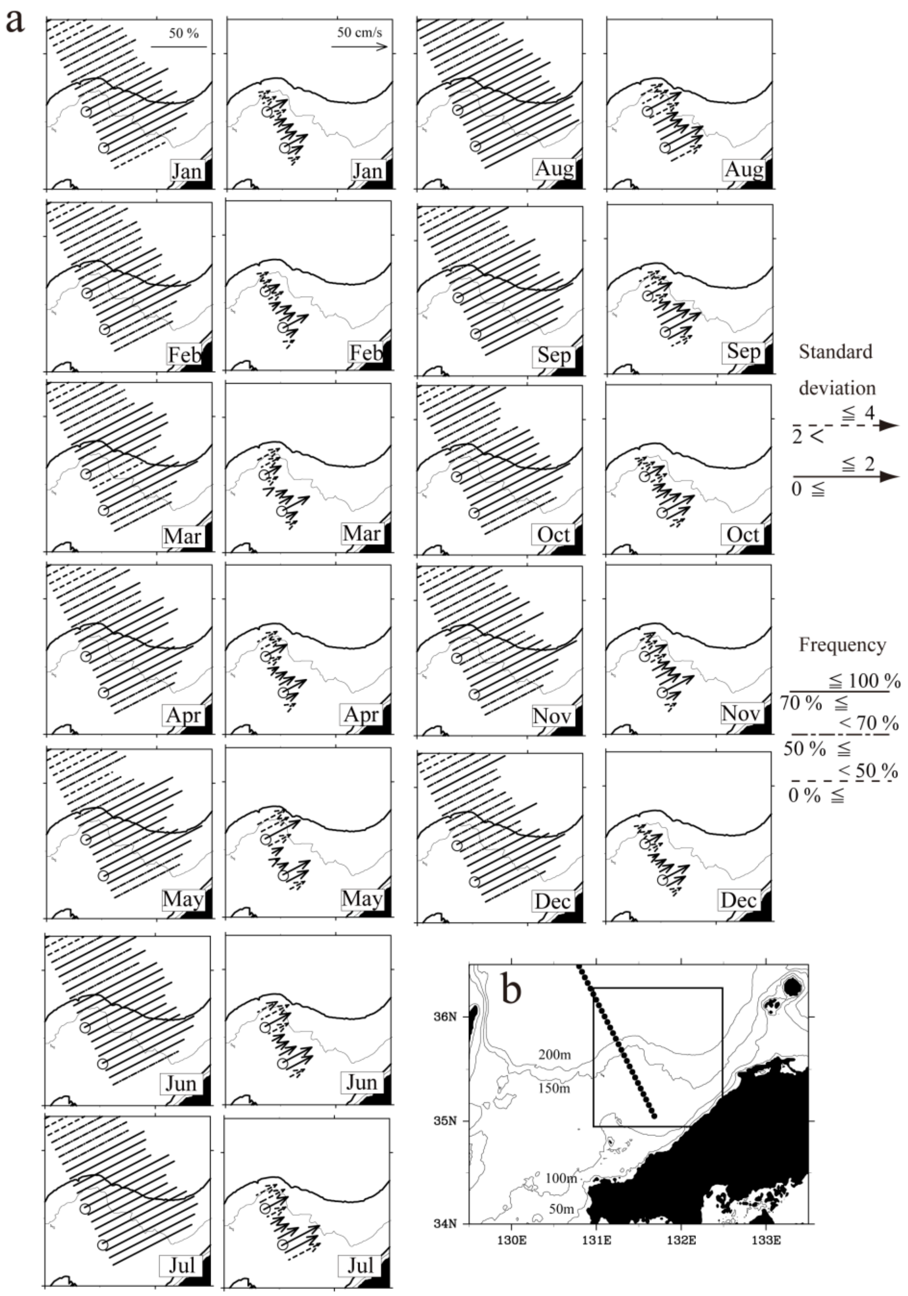

Figure 2.9: (a) Frequency of current (left side) and standard deviation normalized by monthly mean current speed (right side) with monthly mean sea surface current velocity from January to December. In the left panel, solid, dashed–dotted, and dashed lines indicate frequencies of greater than 70%, greater than 50% but less than 70%, and less than 50%, respectively. In the right panel in each month, the solid arrow, broken arrow, and no arrow indicate that the normalized standard deviation of the current is less than 2, greater than 2 but less than 4, and greater than 4, respectively. Open circles indicate current path positions. (b) The open square marks the analyzed area and closed circles indicate satellite altimeter data points. Contour lines show the 50-m, 100-m, 150-m, and 200-m isobaths, respectively.

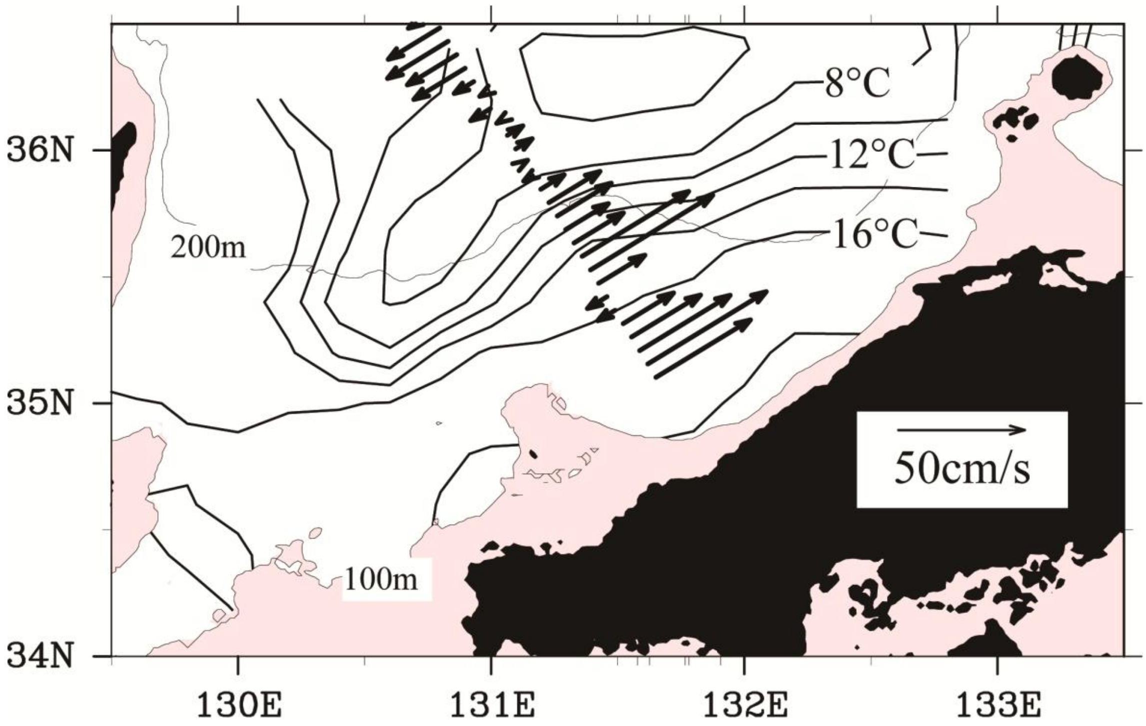

Figure 2.10: Monthly mean current velocities (arrows) perpendicular to the subsatellite track and monthly mean water temperature (thick contour lines) at 100 m depth in July 1995. Thin counter lines indicate water depth.

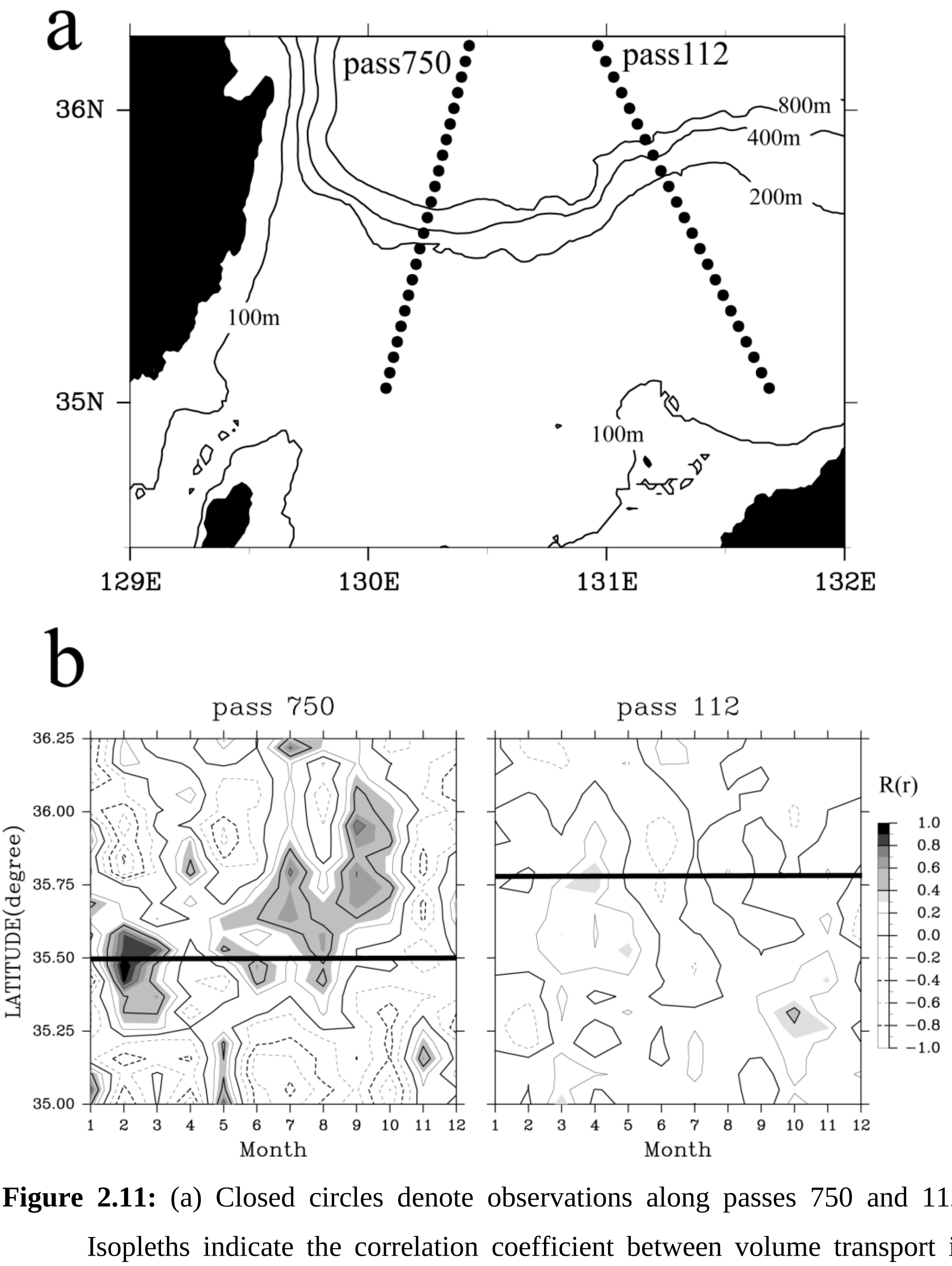

Figure 2.11: (a) Closed circles denote observations along passes 750 and 112. (b) Isopleths indicate the correlation coefficient between volume transport in the western channel of the Tsushima Strait and current velocity perpendicular to passes 750 and 112, respectively (1% significance level, P > 0.2 for pass 750, P > 0.1 for pass 112). The solid line marks the 200-m isobath. Monochrome shading indicates correlation coefficients over 0.3.

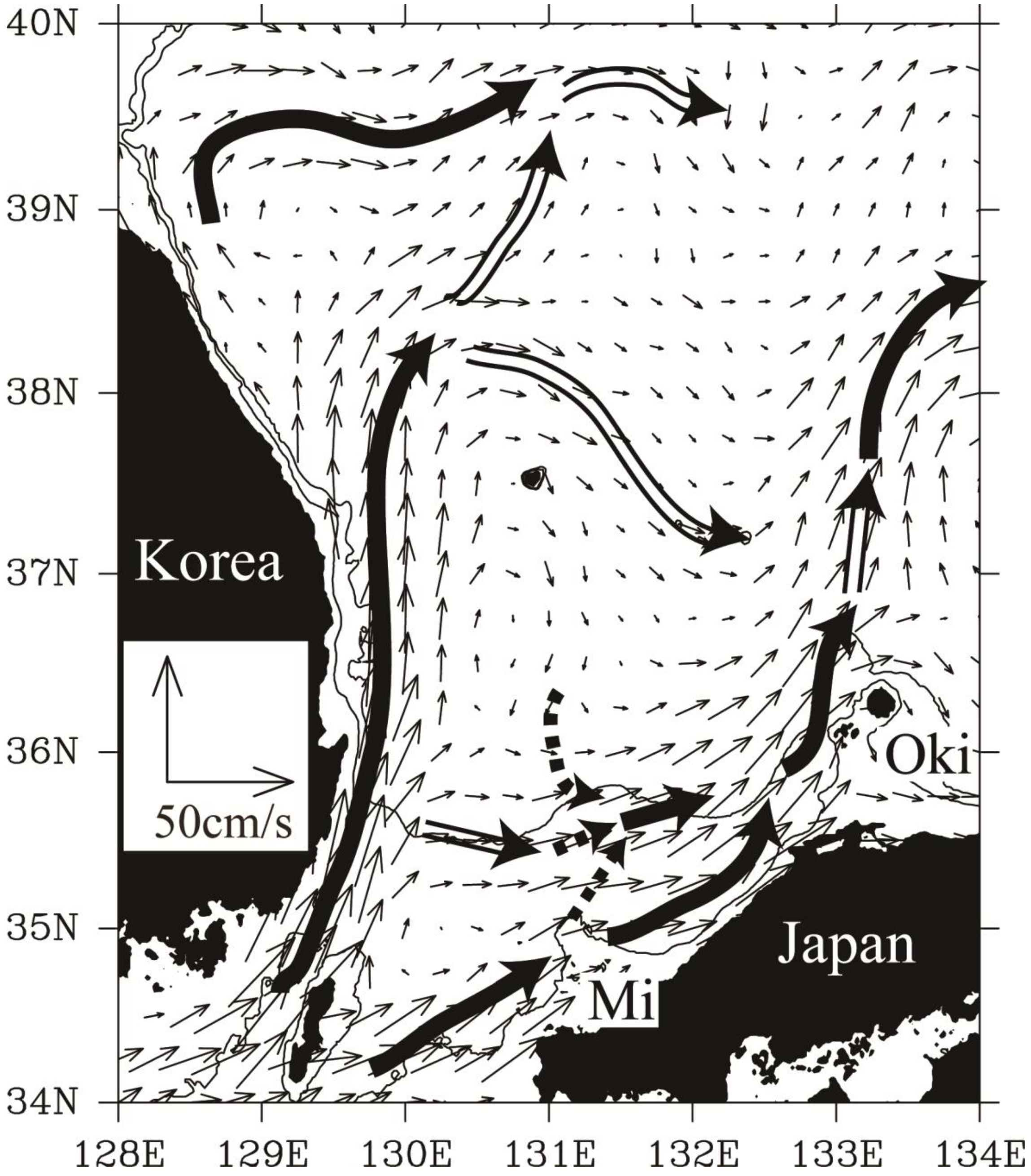

Figure 2.12: Schematic view of TWC paths in the southwestern Japan Sea. Vectors show the mean sea surface current. Thin contour lines indicate the 100-m and 200-m isobaths. Solid arrows indicate stable current paths. Double arrows indicate variable current paths. Broken arrows indicate expected current paths.

Chapter 3

Interannual variation in the TBTWC controlled by winter surface cooling in the Japan Sea - Data analysis -

3.1 Introduction

In the Chapter 2, we revealed that the triple branch current pattern of the Tsushima Warm Current (TWC) in the southwestern part of the Japan Sea by using the absolute sea surface current (ASSC) field data with high spatial and temporal resolution (Fig. 3.1). The third branch of the TWC (TBTWC) path is one of the TWC paths and the TBTWC flows northward along the east coast of Korean Peninsula up to around 38˚N. The seasonal variation of the current path was small, and the TBTWC categorized as stable current by frequency analysis in Chapter 2. Moreover, according to previous studies has been considered that the TBTWC is a western boundary current and the current is relatively stable (Kawabe, 1982a,b; Yoon, 1982). However, Hong and Cho (1983), Kim and Legeckis (1986) and Mitchell et al. (2005) reported that the separation position from the coast of the TBTWC path shifted to lower latitude and the TBTWC disappeared from spring to autumn in 1974, 1981 and 2000, respectively. In our dataset of ASSC field, we could occasionally see that the TBTWC path largely changed in interannual variation. Therefore, we had a question that why TBTWC path changed in interannual and investigate the reason of interannual variation of the TBTWC path.

Naganuma (1985) reported from data analysis of water temperature and wind data that variation in the TWC path coincided well with that in outbreak of winter monsoon from 1953 to 1983. However, they did not make mention of the mechanism. Winter monsoon over the Japan Sea is a driving force of the subarctic circulation in the northern part of the Japan Sea (Kim and Yoon, 1996; Yoon et al., 2005) and gives rise to subduction of the surface water off Vladivostok (Senjyu, 1999; Yun et al., 2004). Moreover, the subduction of cold water around the Russian to North Korean coast might affect the distribution of the cold water off east coast of the Korean Peninsula (Kim and Kim, 1983; Lie, 1991; Yun et al., 2004). The cold water distribution off east coast of the Korean Peninsula might affect the TBTWC path.

Choi et al. (2009) investigated the interannual variation of the TBTWC path using a reduced gravity model. Their result showed that when wind stress curl in winter was larger than that in normal winter, a width of the TBTWC path was wider but separation position from the coast of the TBTWC did not change. Seung and Nam (1991) investigated the effect of the winter cooling on the TBTWC path by mean of a layer model. They showed that winter cooling induced the northward current along the

Korean coast associated with propagating coastal trapped waves. While, Seung and Kim (1989) and Seung (1992) showed from results of simple reduced gravity model that the separation position from the Korean Peninsula of the TBTWC in winter was changed by wind stress curl and surface cooling in winter. They suggested that strong positive wind stress curl and surface cooling induced the positive relative vorticity, and it enhanced the subarctic circulation and North Korean Cold Current (NCC). As a result, the separation position of the TBTWC from the coast shifted to lower latitude. Their results explained the change of separation position of the TBTWC only in winter, and they could not demonstrate observed change of separation position of the TBTWC in spring and summer.

In this chapter, we try to elucidate interannual variation in the TWC path, especially TBTWC path, by analyzing absolute sea surface dynamic height (ASSDH) data which calculated from both satellite altimetry and satellite-tracked drifters data and to examine which parameters such as wind stress curl, surface cooling, and volume transport of the TWC relates to the interannual variation of the TBTWC path.

3.2 Data

3.2.1 Monthly absolute sea surface dynamic height field

We estimated mean sea surface currents and the sea surface dynamic height anomalies in the Japan Sea in Chapter 2. Assuming geostrophic balance, we calculated mean sea surface dynamic height field from the mean sea surface current data. The method is straightforward. The absolute sea surface dynamic height (ASSDH) $H_{abs}(\mathbf{x},t)$ at position **x** and time t can be written as follows:

$$H_{abs}(\mathbf{x},t) = H_{mean}(\mathbf{x}) + H_{anom}(\mathbf{x},t), \tag{3-1}$$

where $H_{mean}(\mathbf{x})$ and $H_{anom}(\mathbf{x},t)$ are mean sea surface dynamic height and the sea surface dynamic height anomaly, respectively. We explain the method of obtaining $H_{mean}(\mathbf{x})$ and $H_{abs}(\mathbf{x},t)$.

We calculate the mean sea surface dynamic height $H_{mean}(\mathbf{x})$ in equation (3-1) from mean sea surface current $V_{mean}(\mathbf{x})$ derived in Chapter 2 assuming geostrophic balance. We set a start point of the calculation at 140°E and 41°N (west of the Tsugaru Strait) because of the some lack of the mean sea surface current data north of 41°N. Mean sea surface dynamic height at the start point defines as zero. Assuming the first approximation of the geostrophic balance, a mean sea surface dynamic height is estimated by the followings;

$$\Delta\eta_R = \frac{f_{(i,j+1/2)} \times \Delta y \times U_{(i,j+1/2)}}{g} - \frac{f_{(i+1/2,j+1)} \times \Delta x \times V_{(i+1/2,j+1)}}{g}, \tag{3-2}$$

$$\Delta\eta_L = \frac{f_{(i+1,j+1/2)} \times \Delta y \times U_{(i+1,j+1/2)}}{g} - \frac{f_{(i+1/2,j)} \times \Delta x \times V_{(i+1/2,j)}}{g} \tag{3-3}$$

where Δx, Δy, f, U, and V indicate the grid interval in the x and y direction, Coriolis parameter at each latitude, and the east-west and north-south current speeds in the grid shown in Fig. 3.2a. Although the mean sea surface height at i+1 and j+1, h(i+1, j+1) calculated by $\Delta\eta_R$ should be equal to that by $\Delta\eta_L$, we occasionally obtained $\Delta\eta_R \neq \Delta\eta_L$ due to the residual ageostrophic component and error in the mean sea surface current. Therefore, a gap $\delta = \Delta\eta_L - \Delta\eta_R$ between h(i+1, j+1), h(i+1, j) and h(i, j+1) distributes to each point as follows. When a δ > 0, h(i+1, j) is $h(i,j) + \Delta\eta_{x(i+1/2,j)} - \frac{\delta}{3}$, h(i, j+1) is $h(i,j) + \Delta\eta_{y(i,j+1/2)} + \frac{\delta}{3}$, and h(i+1, j+1) is $h(i,j) + \Delta\eta_L - \frac{\delta}{3}$. When a $\delta <$ 0, the h(i+1, j) is $h(i,j) + \Delta\eta_{x(i+1/2,j)} + \frac{\delta}{3}$, h(i, j+1) is $h(i,j) + \Delta\eta_{y(i,j+1/2)} - \frac{\delta}{3}$, and h(i+1, j+1) is $h(i,j) + \Delta\eta_R - \frac{\delta}{3}$. The mean sea surface dynamic height field shown in Fig. 3.2b is derived by these methods.

We recalculated the mean sea surface current velocity $V'_{mean}(\mathbf{x})$ from the mean sea surface dynamic height shown in Fig. 3.2b to validate the calculated mean sea surface dynamic height. $V'_{mean}(\mathbf{x})$ was compared with the mean sea surface current $V_{mean}(\mathbf{x})$ estimated in Chapter 2 using the following equation;

$$\Delta A = \frac{\sum_{i=1}^{N} \sqrt{V_{mean}^2(x_i) + V'^2_{mean}(x_i) - 2\left|V_{mean}(x_i)\right|\left|V'_{mean}(x_i)\right|\cos\theta}}{N}. \quad (3\text{-}4)$$

θ is the difference in current direction between $V_{mean}(x_i)$ and $V'_{mean}(x_i)$ at grid point i. N is the total number of grid points. ΔA is 0.03 ms^{-1}. The sea surface dynamic height has sufficient accuracy to investigate TWC current variations because the mean current velocity of the TWC is approximately 0.20 ms^{-1}.

Finally, we calculated the monthly ASSDH shown as $H_{abs}(\mathbf{x},t)$ in equation (1) from May 1995 to October 2010 by adding the mean sea surface height $H_{mean}(\mathbf{x})$ and the sea surface dynamic height anomaly $H_{anom}(\mathbf{x},t)$.

3.2.2 Data processing for the other data

Daily wind stress curl data from the QSCAT/NCEP blended ocean wind data with a resolution of 0.5° × 0.5° were downloaded from Colorado Research Associates ver. 5.0 (data products and documentation are available online from the CISL research data archive at http://rda.ucar.edu/datasets/ds744.4/#!description). The daily data were averaged for each month from July 1999 to July 2009. Water temperature data from the World Ocean Database 2009, Korean Ocean Data Center, and the Korean Meteorological Administration were used to create monthly mean distributions of water temperature in the Japan Sea and a cross-section of the Tsushima Strait. The water temperature data were interpolated horizontally and vertically onto a 0.25° of latitude and longitude using an objective interpolation method. Net heat flux data from January 1995 to December 2006 with a resolution of 1° × 1° were derived from the ver. 2 of the

Japanese Ocean Flux data sets with the use of remote sensing observations (J-OFURO2) (Tomita and Kubota, 2010). Volume transport of the TWC through the Tsushima Strait from January 1995 to December 2009 was estimated from sea level data using the method of Takikawa and Yoon (2005).

3.3 Variations in the TBTWC path

3.3.1 Seasonal and interannual variation in the TWC

The TWC paths have large temporal and spatial variability in the Japan Sea (Morimoto and Yanagi, 2001), and it is difficult to determine the current path pattern objectively. EOF analysis was applied to the ASSDH data for 16 years to examine the characteristics of temporal and spatial variations in the TWC path pattern. Kim and Yoon (2010) pointed out that when EOF analysis is applied to ASSDH data in the entire Japan Sea, the variations in the sea surface circulation in the northern part of the Japan Sea are significantly influenced by the considerable seasonal variation in surface circulation in the southern part of the Japan Sea. Therefore, we divided the area into two areas at 41°N, the northern and southern part of the Japan Sea, based on the mean sea surface current and result of Kim and Yoon (2010) (Fig. 3.1).

Each mode of EOF analysis in the present study is an unconventional decomposition of the spatial variance. This method can manifest the variance associated with frontal, eddy, and jet structures which are often clearly evident (Lagerloef and Bernstein, 1988; Morimoto and Yanagi, 2001; Kim and Yoon, 2010).

The EOF decomposition of the ASSDH in the southern part of the Japan Sea yielded two dominant modes explaining 79% and 9% of the total variance, respectively. As the other modes contributed less than a few percent of the total variance, the first and second in the southern part of the Japan Sea will be discussed in this section.

Figure 3.3a shows the spatial structure of the EOF 1st mode of the ASSDH. The spatial structure is almost the same as the mean sea surface dynamic height $H_{mean}(\mathbf{x})$ shown in Fig. 3.2b and reflects the TWC current path pattern from the Tsushima Strait to the Tsugaru Strait. A time series of the EOF 1st mode was always positive and had seasonal variation (Fig. 3.3b). Monthly averaged time series of the EOF 1st mode indicated a minimum in April and a maximum in August (Fig. 3.3c). Therefore, the EOF 1st mode showed strong and weak TWC with seasonal variations.

The spatial structure and time series of the EOF 2nd mode are shown in Fig. 3.4a and b. The spatial structure indicated variations in the TWC path off the east coast of the Korean Peninsula, northwest and north of the Noto Peninsula (Fig. 3.4a). The largest amplitude was observed off the east coast of the Korean Peninsula, and variations in this region may indicate variability in the TBTWC path. The interannual variations were dominant in the time series of the EOF 2nd mode (Fig. 3.4b), and the seasonal variation was small in the EOF 2nd mode (Fig. 3.4c). Combining mean sea surface current shown in Fig. 3.2b and EOF 2nd mode multiplied spatial structure and the time constant, we rebuild the sea surface currents in September 2000 in which the time constant of the EOF 2nd mode is small and October 2001 in which the time constant of the EOF 2nd mode is large (Fig. 3.5). In these figures, the separation position of the TBTWC from the Korean coast was 37°N in September 2000 and 38.5°N in October 2001, respectively. The EOF 2nd mode indicated the interannual variation in the separation position of the TBTWC from the Korean Peninsula.

3.3.2 Variation factor for the separation position of the TBTWC from the Korean Peninsula

To investigate the cause of interannual variations in the TBTWC path, we investigated the relationship between the EOF 2nd mode of ASSDH and parameters such as heat flux, wind stress curl, and volume transport of the TWC. Time constants of EOF 2nd mode were averaged from December to March, and the averaged data were regarded as winter data of the EOF 2nd mode. The time constant in each month from April to November was also averaged, and was regarded as the monthly mean data of the EOF 2nd mode. Net heat flux and wind stress curl over the northern part of the Japan Sea in winter were spatially averaged, and are called winter NHF and winter curl (τ), respectively. We also used a volume transport data in the western channel of the Tsushima Strait (Western TS) and total volume transport data for the Tsushima Strait (Total TS). The area of northern Japan was defined as shown in Fig. 3.1.

We calculated the lag correlation and correlation coefficients between the monthly averaged time constants of the EOF 2nd mode (SJS mode 2) and the winter NHF, the winter curl (τ), the western TS, and the total TS, respectively (Table 3.1). The highest correlation was observed between SJS mode 2 and Winter NHF in all parameters. The lag correlations between the SJS mode 2 and Winter NHF were high from April until July and insignificant from August to November (95% confidence limit [CL], $R > 0.55$). From December to March, we recalculate correlation coefficient between time constants of 2nd mode and Winter NHF. Winter NHF used in December is the area average of net heat flux over the northern Japan Sea in December, Winter NHF used in January is average in December to January, and Winter NHF used in February is average in December to February. After March, Winter NHF is average in December to March. Significant relations were obtained from January. Figure 3.6a and b show the interannual variation in the Winter NHF and SJS mode 2. Both variation patterns are similar. Moreover, the value of SJS mode 2 became larger from April to July, particularly in 1996, 2000, 2002, and 2005. This result suggests that the separation position of the TBTWC from the Korea Peninsula moves to more south (north) when surface cooling in the northern part of the Japan Sea in winter is strong (weak). Although there were relatively high correlations between SJS mode 2 and total TS in July and August, the correlations between SJS mode 2 and the other parameters were quite low.

Water temperatures at a depth of 100 m were composited to the cases of strong and weak surface cooling to investigate how surface cooling in winter affects the hydrographic conditions east of the Korean Peninsula. Figure 3.7a and b are the composite water temperatures at 100-m depth of weak winter cooling (winter NHF > -220 Wm^{-2}) and strong winter cooling (winter NHF < -270 Wm^{-2}), respectively. Cold-water masses < 6°C spread around the east coast of the Korean Peninsula toward the summer time in both cases. The cold-water mass of the case for strong winter cooling is more spread than that of the case for weak winter cooling. This observation suggests that surface cooling during winter in the northern part of the Japan Sea metamorphoses the hydrographic conditions off the east coast of the Korean Peninsula, and such variation results in a variation in the TBTWC path.

We focused on variations in the current field in the northern part of the Japan Sea to understand the relationship between cold-water mass expansion off the east coast of the Korean Peninsula and winter surface cooling. We applied EOF analysis to the sea surface dynamic height anomaly data in the northern Japan Sea to identify the dominant current patterns. We could not use the ASSDH data in this region because mean sea surface dynamic height was not estimated due to the lack of the mean sea surface current data there. The EOF decomposition yielded a dominant mode explaining 17% of the total variance. The other modes contribute less than a few percent of the total variance. The spatial structure and its time series of the EOF 1st mode are shown in Fig. 3.8. The spatial structure of the EOF 1st mode shows a current along the Primorye coast (Fig. 3.8a). The time constant of the EOF 1st mode takes both positive and negative values, and seasonal variation is dominant (Fig. 3.8b). The monthly averaged time constant of the EOF 1st mode indicates a maximum in autumn and minimum in spring (Fig. 3.8c). The standard deviation of the time constant for each month was relatively large, suggesting that interannual variations are also included in the mode. The Liman Cold Current flows along the Primorye coast throughout the year (Yarichin, 1980). The EOF 1st mode indicates strong and weak Liman Cold Currents with seasonal and interannual variation.

The time constants of the EOF 1st mode were averaged from December to March as winter data and in each month as monthly data (NJS mode1). We investigated the relationship between NJS mode 1 and SJS mode 2, winter NHF, and winter curl (τ). The correlation coefficients between the NJS mode1 and SJS mode 2 from April to July were high and significant (95%CL, R > 0.49) (Table 3.3). The NJS mode1 also had a high lag correlation with winter NHF from April to May (95%CL, R > 0.55). In contrast, correlations between NJS mode 1 and winter curl (τ) were low and insignificant (95% CL, R > 0.60).

Correlation analyses suggested that the interannual variation in the separation position of the TBTWC related to strong and weak variations in the Liman Cold Current. In addition, the strong and weak condition of the Liman Cold Current in spring might be caused by variations in surface cooling in winter. These results imply the following processes. The Liman Cold Current is intensified by stronger winter cooling compared to a normal year, and then a greater amount of cold water is transported to off the Korean coast by the current. As a result, the cold-water mass off the Korean coast expands into a wider area. The TBTWC adjusts the density distribution off the Korean coast and separates from the coast at lower latitude. There might be time lag between intensification of the Liman Cold Current and transport of the cold-water mass off the Korean coast. Hence, it seems that the separation position of the TBTWC from spring to summer was highly correlated with surface cooling in the northern part of the Japan Sea in winter.

3.4 Summary

We analyzed ASSDH data, which are derived from satellite altimeter and satellite-tracked drifter, to clarify the mechanism of the interannual variation in the TBTWC path, particularly the separation position of the TBTWC from the Koran Peninsula in summer. The EOF 2^{nd} mode of the ASSDH in the southern part of the Japan Sea denotes interannual variations in the TBTWC and TWC. Monthly averaged time constants of the EOF 2^{nd} mode from spring to summer correlated with surface cooling in winter averaged in the northern part of the Japan Sea. This result suggests that the interannual variations of the separation position of the TBTWC from spring to summer is caused by surface cooling in winter in the northern part of the Japan Sea. The EOF 1^{st} mode of the ASSDH in the northern part of the Japan Sea, which denotes strong and weak condition of the Liman Cold Current, also had a high correlation with surface cooling in winter averaged in the northern part of the Japan Sea. Correlation analyses suggested that the interannual variation of the TBTWC, particularly the separation position of the TBTWC from the Korean Peninsula, was related to strong and weak variation in the Liman Cold Current. In addition, strong and weak Liman Cold Current in the spring might be caused by variations in surface cooling during winter.

Table 3.1: Correlation coefficients between time constants of the empirical orthogonal function (EOF) 2^{nd} mode in the winter and in each month and Winter NHF, Winter Curl (τ), western TS, and total TS. Winter NHF is the area average of net heat flux over the northern Japan Sea in winter, winter curl (τ) is the area average of winter wind stress curl over the northern Japan Sea, western TS is the volume transport of the western channel of the Tsushima Strait each month, and total TS is the total volume transported in the Tsushima Strait each month.

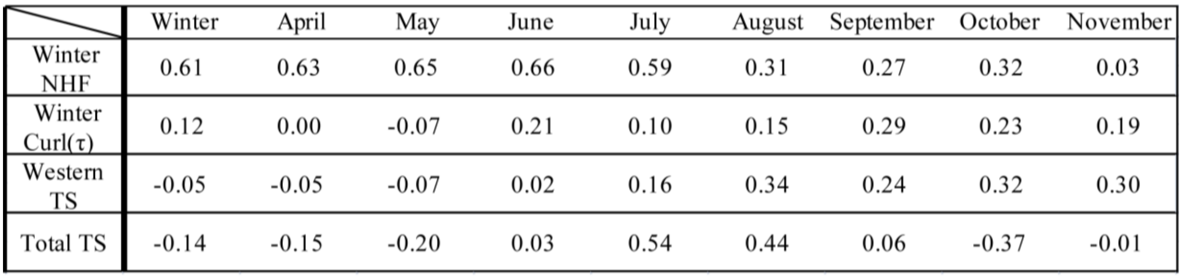

	Winter	April	May	June	July	August	September	October	November
Winter NHF	0.61	0.63	0.65	0.66	0.59	0.31	0.27	0.32	0.03
Winter Curl(τ)	0.12	0.00	-0.07	0.21	0.10	0.15	0.29	0.23	0.19
Western TS	-0.05	-0.05	-0.07	0.02	0.16	0.34	0.24	0.32	0.30
Total TS	-0.14	-0.15	-0.20	0.03	0.54	0.44	0.06	-0.37	-0.01

Table 3.2: Correlation coefficients between time constants of the empirical orthogonal function (EOF) 2nd mode in each month and Winter NHF until September. Winter NHF is the area average of net heat flux over the northern Japan Sea in winter. Winter NHF used in December is the area average of net heat flux over the northern Japan Sea in December, Winter NHF used in January is average in December to January, Winter NHF used in February is average in December to February. After March, Winter NHF is average in December to March.

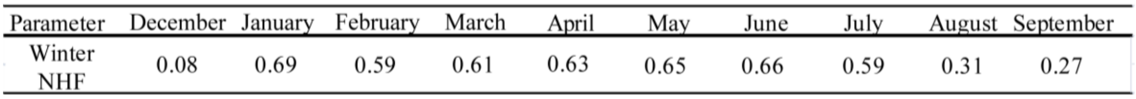

Parameter	December	January	February	March	April	May	June	July	August	September
Winter NHF	0.08	0.69	0.59	0.61	0.63	0.65	0.66	0.59	0.31	0.27

Table 3.3: Correlation coefficients between time constants of empirical orthogonal function (EOF) 1st mode in winter and each month and monthly averaged time constants of the EOF 2nd mode (SJS mode 2), winter NHF, and winter curl (τ). SJS mode 2 is the monthly averaged time constant of EOF 2nd mode of absolute sea surface dynamic height (ASSDH) in the southern part of the Japan Sea. Winter NHF is the area average of net heat flux over the northern Japan Sea in winter, and winter curl (τ) is the area average of winter wind stress curl over the northern Japan Sea.

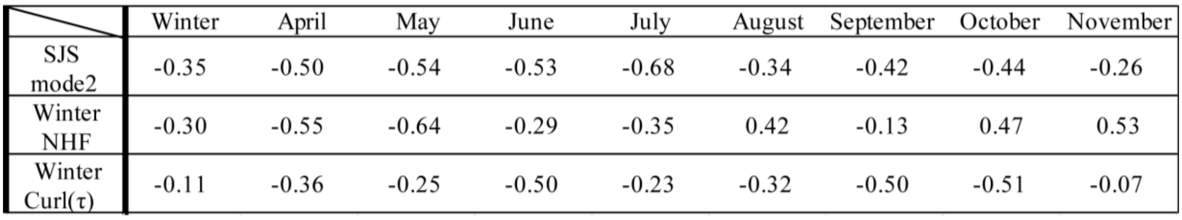

	Winter	April	May	June	July	August	September	October	November
SJS mode2	-0.35	-0.50	-0.54	-0.53	-0.68	-0.34	-0.42	-0.44	-0.26
Winter NHF	-0.30	-0.55	-0.64	-0.29	-0.35	0.42	-0.13	0.47	0.53
Winter Curl(τ)	-0.11	-0.36	-0.25	-0.50	-0.23	-0.32	-0.50	-0.51	-0.07

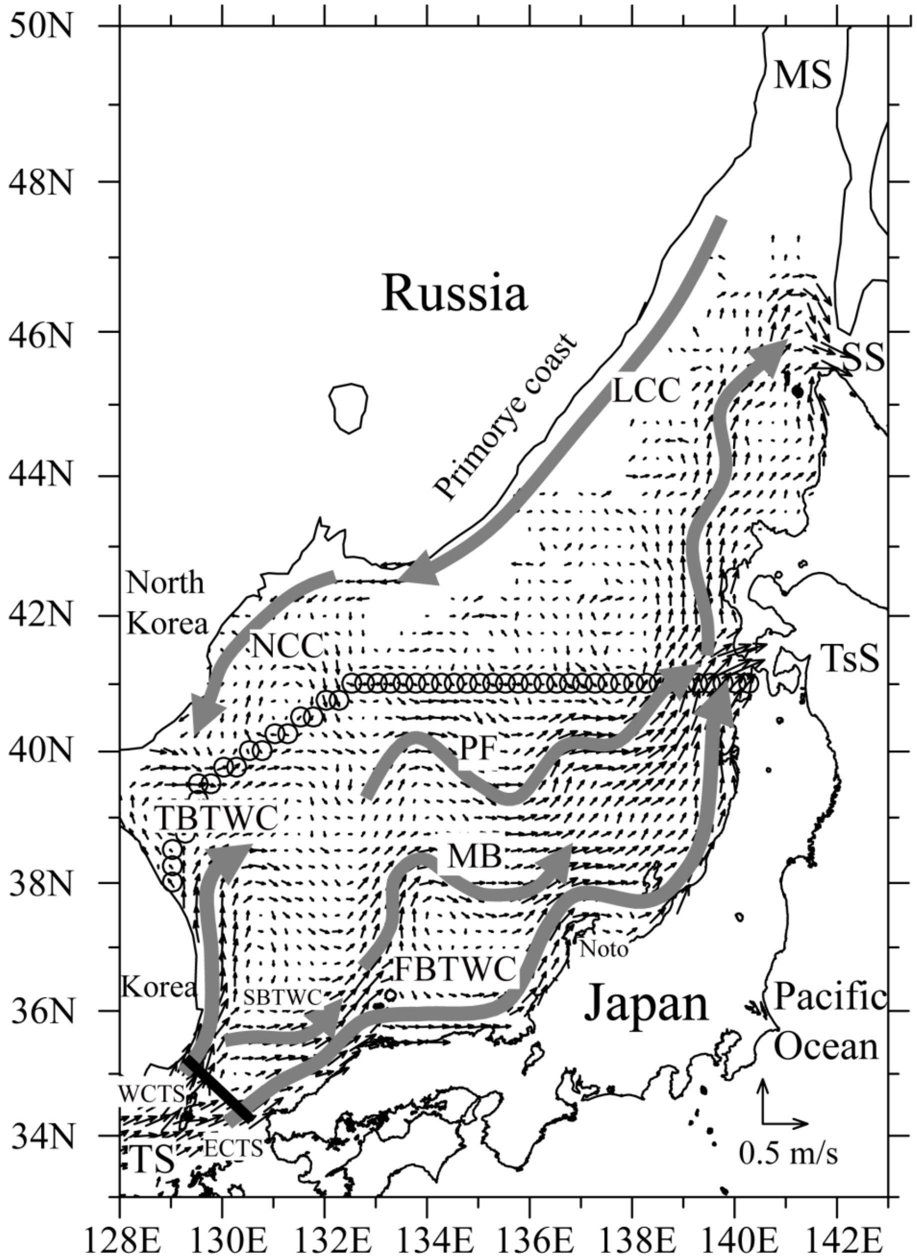

Figure 3.1: Same of Fig. 2.3. Gray arrows represent the current paths which revealed in Chapter 2 and after Mooers et al., 2006. Gray arrows represent the current paths. Vectors show the mean sea surface current field in the Japan Sea during May 1995 through October 2010. A solid line in the Tsushima Strait indicates the cross section of the Tsushima Strait. Circles indicate the boundary of the southern and northern part of the Japan Sea.

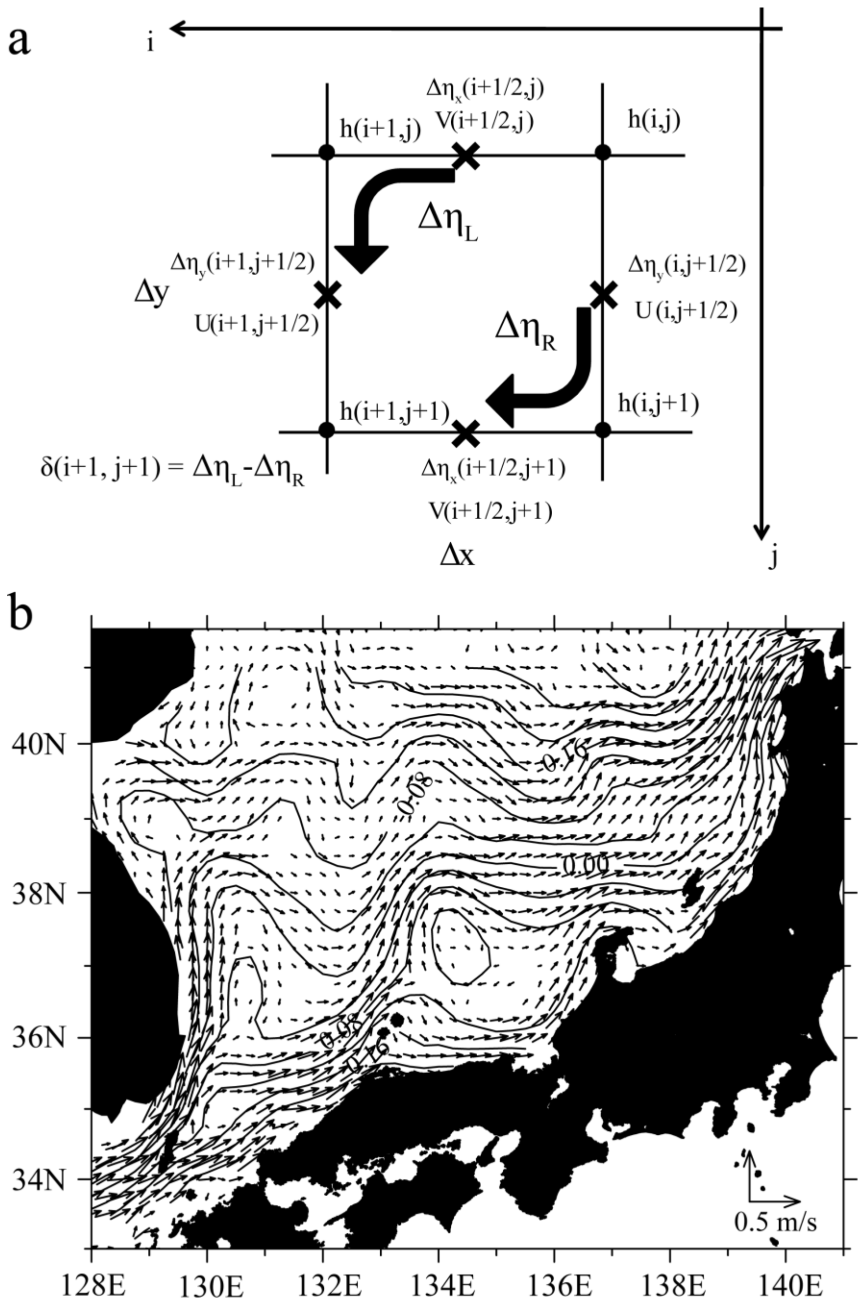

Figure 2

Figure 3.2: (a) Schematic diagram of calculation of the mean sea surface dynamic height. i and j are the unit vectors of the x and y. h is the sea surface height. $\Delta\eta_x$, $\Delta\eta_y$, and V and U are the elevations of the x and y directions and velocities in the i and j directions, respectively. The elevation of $\Delta\eta_R$ and $\Delta\eta_L$ are the integrated heights of the clockwise and anticlockwise directions. δ indicates the difference between $\Delta\eta_L$ and $\Delta\eta_R$. (b) Mean sea surface current and mean sea surface dynamic height from May 1995 to October 2010. Vectors show current velocities of more than 0.03 ms^{-1}.

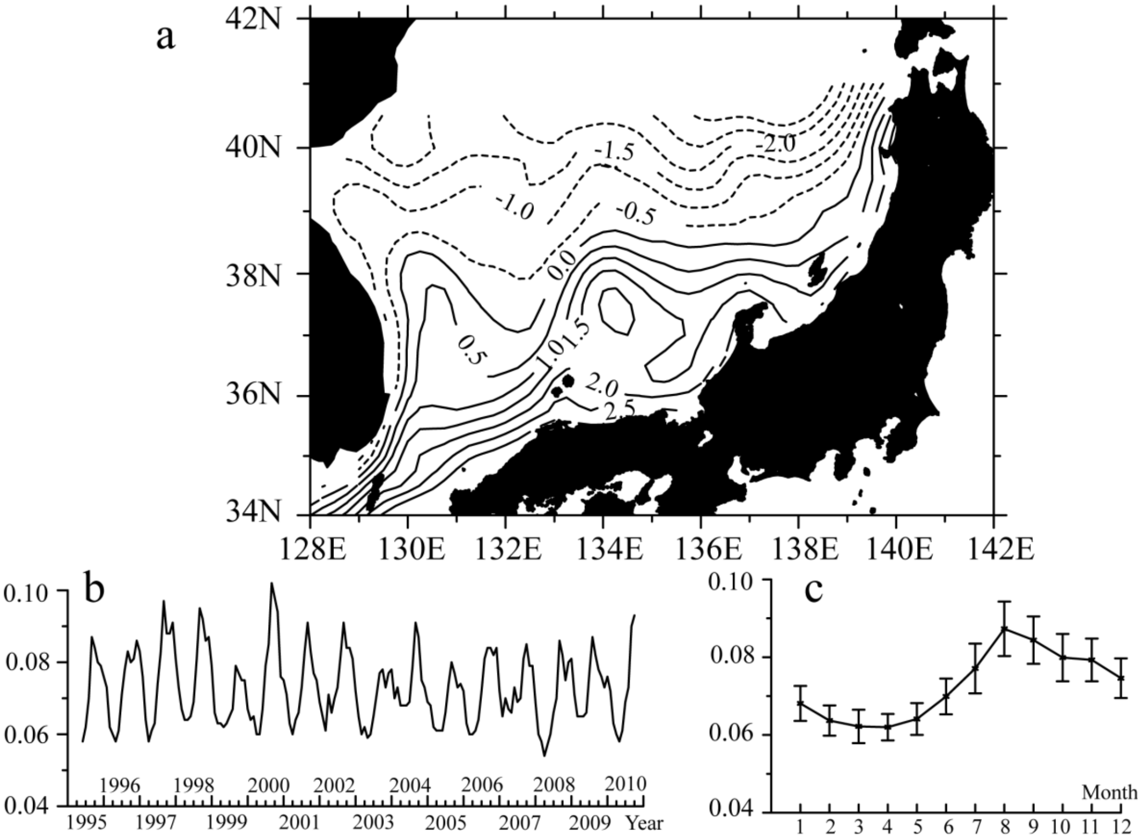

Figure 3.3: Empirical orthogonal function (EOF) 1st mode of the absolute sea surface dynamic height (ASSDH) in the southern part of the Japan Sea. (a) Spatial structure of EOF 1st mode, (b) temporal variation of time constant of EOF 1st mode, and (c) time series of monthly averaged time constants of EOF 1st mode. Error bars in (c) are standard deviations.

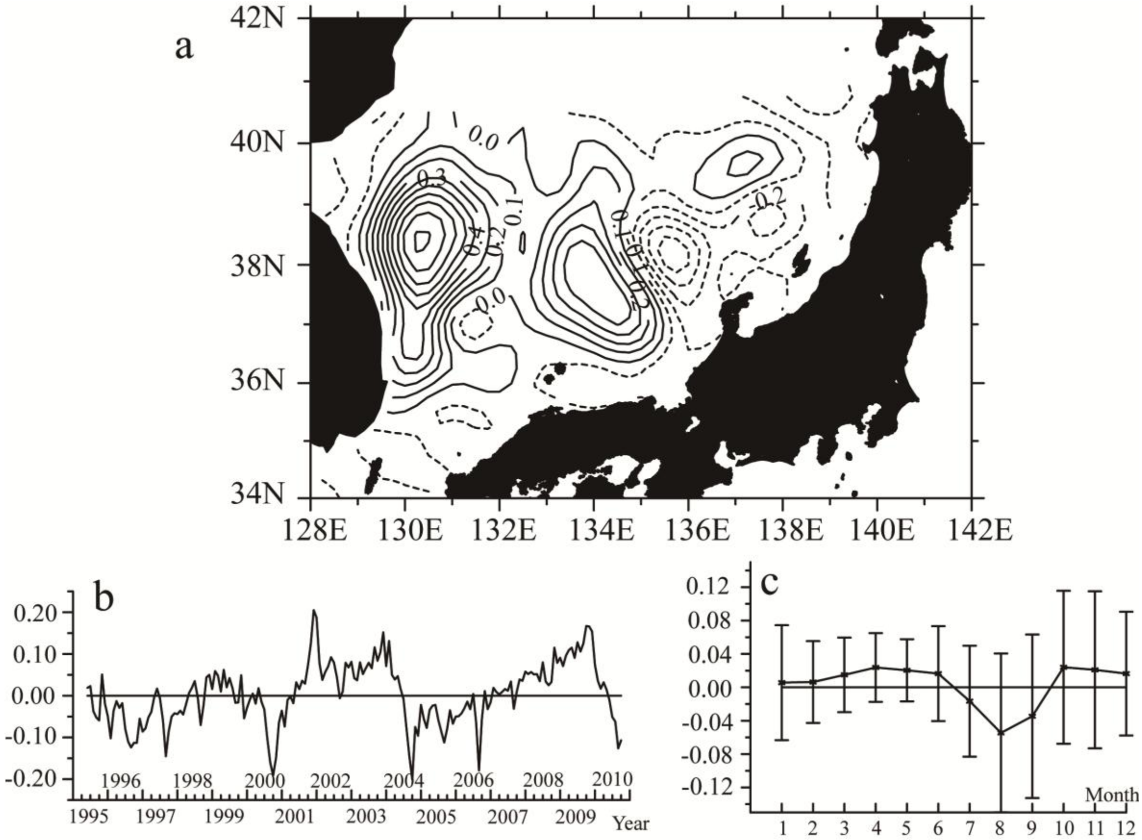

Figure 3.4: Same as Fig. 3.3 but empirical orthogonal function (EOF) EOF 2nd mode of the absolute sea surface dynamic height (ASSDH) in the southern part of the Japan Sea.

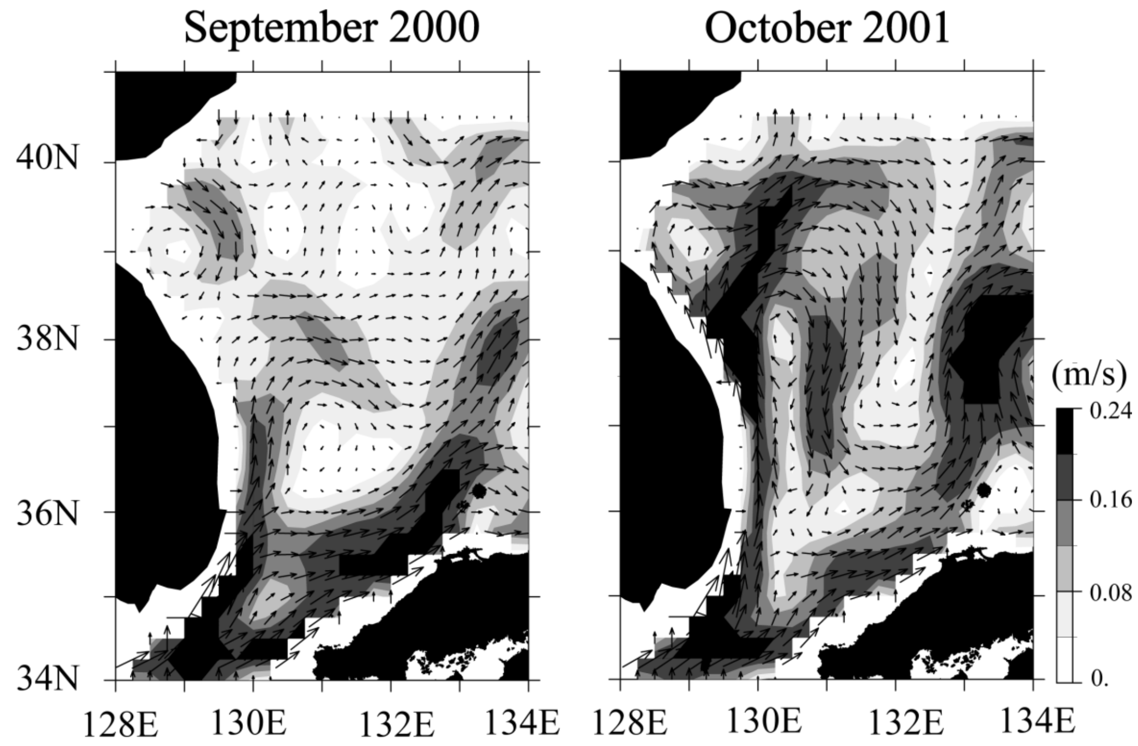

Figure 3.5: Sea surface current in September 2000 and October 2001 reconstructed from empirical orthogonal function (EOF) 2nd mode and the mean sea surface current.

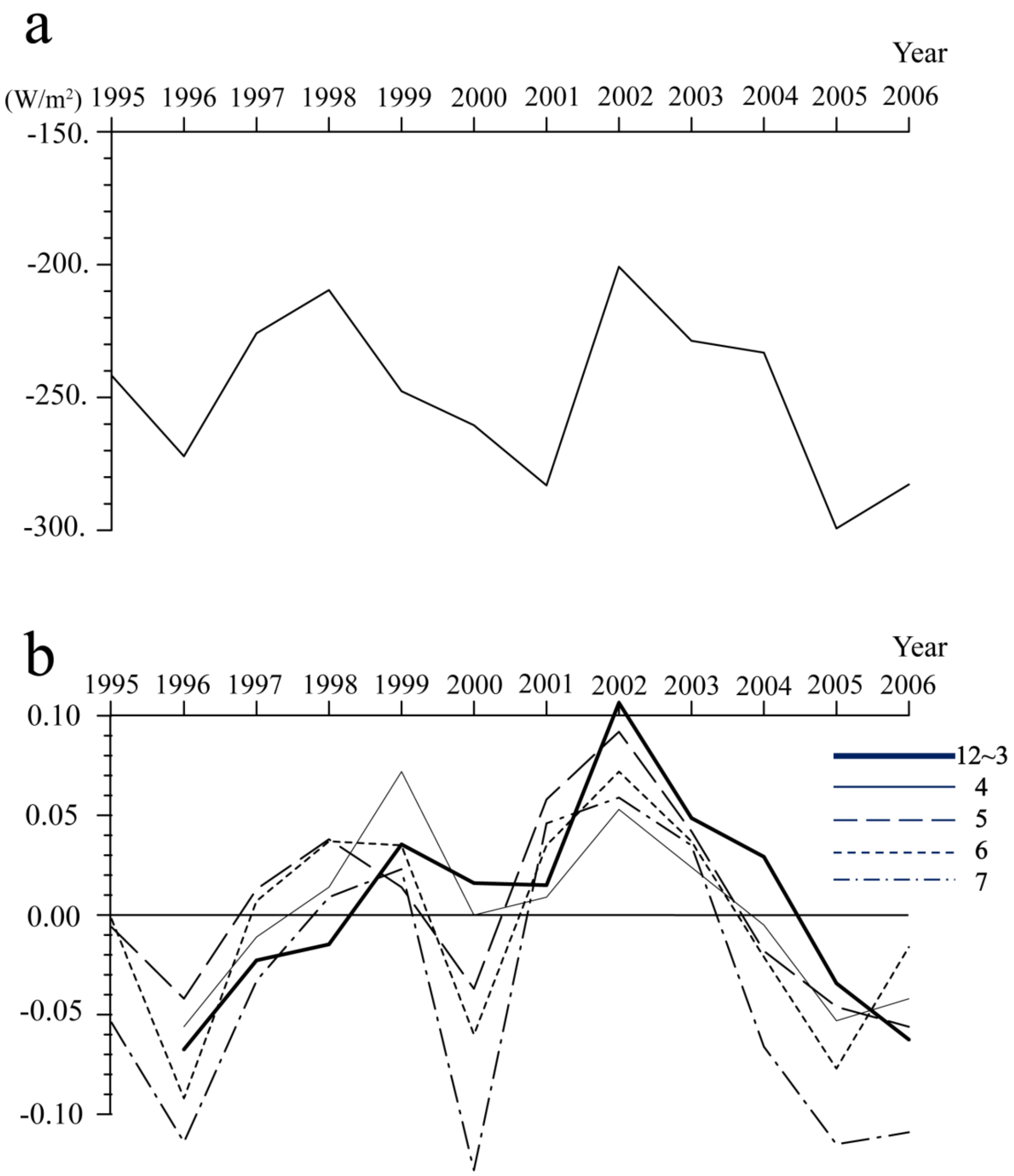

Figure 3.6: (a) Interannual variation of the area averaged net heat flux over the northern Japan Sea. (b) Interannual variation of time constants of empirical orthogonal function (EOF) 2nd mode in winter, April, May, June, and July.

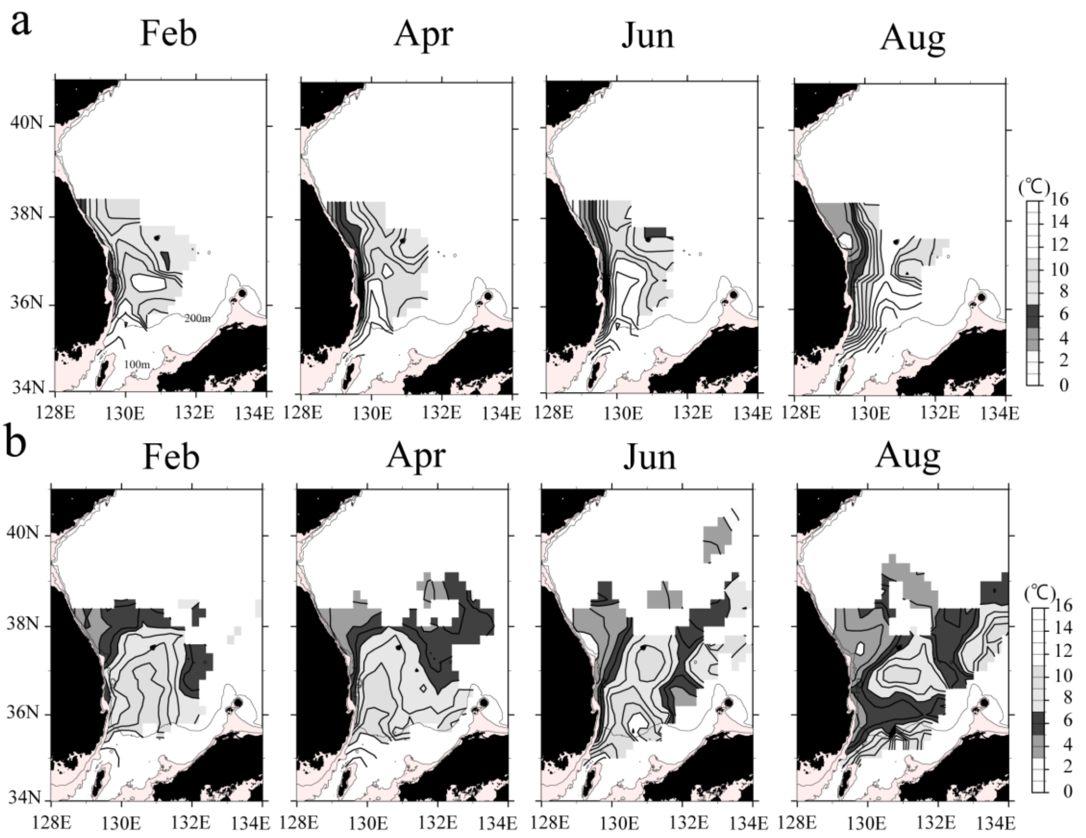

Figure 3.7: Composite water temperature distribution at 100-m depth in (a) weak surface cooling years (over −220 Wm^{-2}) and (b) strong surface cooling year (less −270 Wm^{-2}) in February, April, June, and August.

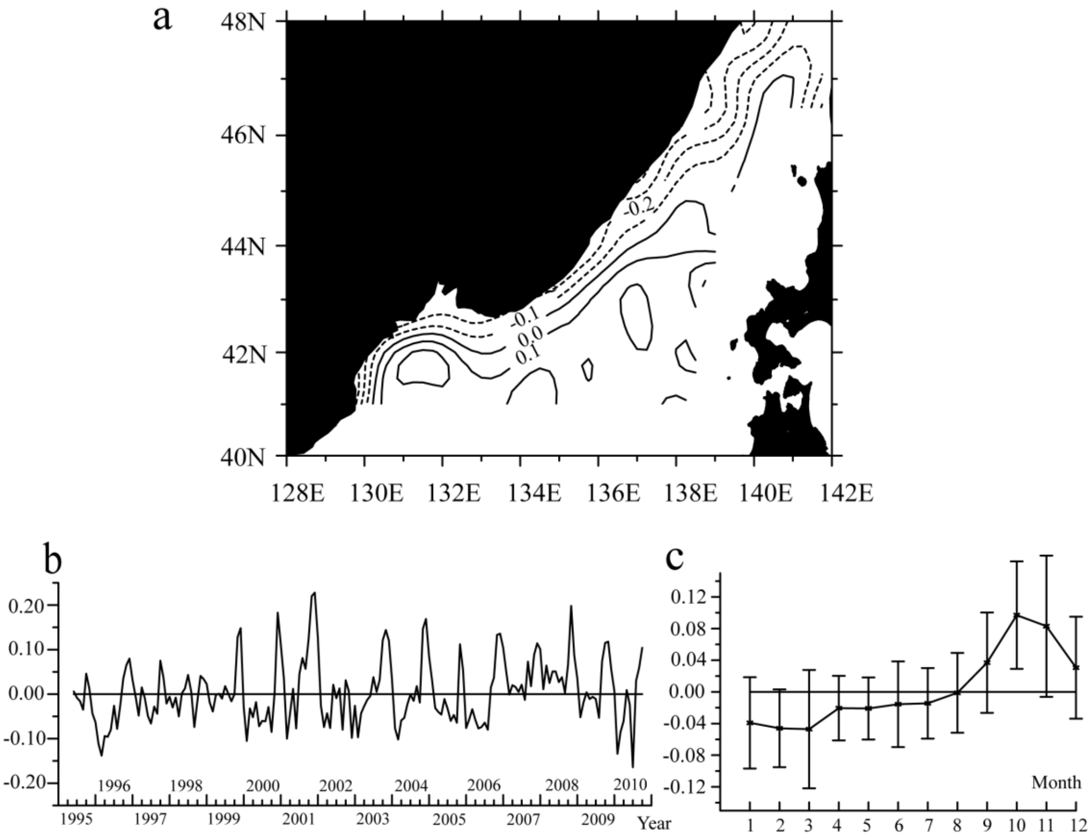

Figure 3.8: Empirical orthogonal function (EOF) 1st mode of the sea surface dynamic height anomaly in the northern part of the Japan Sea. (a) Spatial structure of EOF 1st mode, (b) temporal variation of time constant of EOF 1st mode, and (c) time series of monthly averaged time constant of EOF 1st mode. Error bars in (c) are standard deviations.

Chapter 4

Interannual variation in the TBTWC controlled by winter surface cooling in the Japan Sea - Numerical experiment -

4.1 Introduction

In this chapter, we investigate the mechanism of high correlation between interannual variation in the third branch of the Tsushima Warm Current (TBTWC) path and spatially averaged surface cooling in the northern part of the Japan Sea in winter, that is, why separation position of the TBTWC from the Korean Peninsula becomes lower latitude in summer with about half a year time lag to surface cooling?

Data analysis in previous chapter implied the following processes; 1) the Liman Cold Current is intensified by stronger winter cooling, and then 2) more amount of cold water mass is transported to off Korean coast by the current. Additionally, 3) the cold water mass off Korean coast expand in wider area. 4) The TBTWC adjusts the density distribution off Korean coast and separates from the coast at lower latitude. It is noteworthy that there is about half a year time lag between intensification of the Liman Cold Current by winter surface cooling and transport of cold water mass to off Korean coast.

First process was investigated with use of simple numerical model result by Seung and Kim (1989) and Seung (1992). However, second to fourth processes were suggested from correlation analysis and were not understood their mechanical processes. Therefore, we confirm the above hypothetical process by mean of a reduced gravity model.

4.2 Description of the model

We use a reduced gravity model modified in the Princeton Ocean Model (Blumberg and Mellor, 1987). The topography and boundary conditions of the model were simplified; rectangular shape and inflow and outflow straits in the southwestern and eastern side were set up (Fig. 4.1a). The southwestern and eastern open boundaries corresponded to the Tsushima and Tsugaru Straits, respectively. The numerical model has a two-layer ocean with a motionless deep layer as shown in Fig. 4.1b. Orthogonal coordinates were taken, and the x and y axes are rotated anticlockwise by 25° (Fig. 4.1a). Although the axes are rotated, we regarded the x and y directions as east and north directions for convenience. The grid size is 10 km considering 19 km of the baroclinic Rossby radius of deformation, and the time step is 2 min, which satisfies the

Courant–Friedrichs–Lewy condition. The governing equations are given by:

$$\frac{du}{dt} - fv = -\frac{\partial p}{\partial x} + A_h \nabla^2 u + ru\,, \tag{4-1}$$

$$\frac{dv}{dt} + fu = -\frac{\partial p}{\partial y} + A_h \nabla^2 v + rv\,, \tag{4-2}$$

$$\frac{\partial h}{\partial t} + \frac{\partial hu}{\partial x} + \frac{\partial hv}{\partial y} = -\lambda(h - H)\,, \tag{4-3}$$

$$\frac{dT}{dt} = K_h \nabla^2 T + \frac{Q}{\rho h c_p} + \lambda(h - H)\frac{(T - T_0)}{h}\,, \tag{4-4}$$

where d/dt is the Lagrange derivative, u and v are horizontal components of velocity in the x and y directions, f is the Coriolis parameter at each latitude of the grid, A_h and K_h are the horizontal viscosity and diffusive coefficient (800 $m^2 s^{-1}$), r is the internal frictional coefficient (10^{-7} s^{-1}) , λ is Newtonian dumping (0.2 $year^{-1}$), h is the thickness of the upper layer, T and T_0 are temperatures in the upper and lower layers (T_0 = 1°C), Q is the heat flux through the sea surface with positive (negative) suggesting that the sea surface are heating (cooling), and c_p is the specific heat (4.18 $JK^{-1}gr^{-1}$). ∇^2 is the Laplacian operator in the horizontal direction. In equation (4-3), λ is the inverse of thermal damping time and H is the interface depression associated with the basic buoyancy structure (150 m). This type of expression was used by Davey (1983) and Kim and Yoon (1996). This parameterization is interpreted as meaning that the thermal damping of excess buoyancy over that of the basic buoyancy structure, $(h - H)$, is eliminated by interior mixing (Kawase, 1987).

Because water temperature, T, can vary in the x and y directions, the pressure gradient in the upper layer depends on both the upper-layer thickness, h, and the upper-layer density ρ; i.e.,

$$\nabla p = \nabla(g'h) + \left(\frac{gh}{2\rho}\right)\nabla\rho = \frac{1}{h}\nabla\left(\frac{g'h^2}{2}\right) \quad \text{(McCreary et al., 1997)}, \qquad (4\text{-}5)$$

$$g' = g(\rho_0 - \rho)/\rho_0\,, \qquad (4\text{-}6)$$

$$\rho = \rho_0(1 - \alpha T)\,, \qquad (4\text{-}7)$$

where g' is the reduced gravity, ρ is the upper-layer density, ρ_0 is the lower-layer density (1 $\mathrm{kgm^{-3}}$), α is the coefficient of the expansion (0.25×10^{-3} $°\mathrm{C}^{-1}$), and g is the gravity acceleration (9.8 $\mathrm{ms^{-2}}$). We refer to $P = g'h^2/2$ as the depth-integrated pressure of the upper layer.

Boundary conditions with seasonal variation were applied at the southwestern boundary (Tsushima Strait) based on the observed data (Fig. 4.2). Total volume transport through the Tsushima Strait was approximated by the following equation referred to in Takikawa and Yoon (2005);

$$V_O(t) = V_m + V_1\cos(2\pi t/T_1) + V_2\sin(2\pi t/T_1) + V_3\cos(2\pi t/T_2) + V_4\sin(2\pi t/T_2)\,, \qquad (4\text{-}8)$$

where $V_m = 2.5$ Sv, $V_1 = -0.25$ Sv, $V_2 = -0.19$ Sv, $V_3 = -0.32$ Sv, $V_4 = -0.08$ Sv (1 Sv = 1×10^6 $\mathrm{m^3s^{-1}}$), $T_1 = 360$ days, $T_2 = 180$ days. Water temperature at the boundary was determined by the average of observed data in the Tsushima Strait and approximated by the following equation;

$$T_O(t) = T_m + T_a \sin(2\pi t / T_1 - \pi)\,, \tag{4-9}$$

where T_m =16 °C, T_a=3.5°C. Net heat flux over the domain is approximated by the following equation, which is based on J-OFURO2 net heat flux data;

$$Q_O(t) = Q_m + Q_A \sin(2\pi t / T_1 - \pi / 2)\,, \tag{4-10}$$

where $Q_m = -100$ Wm^{-2}, $Q_A = 200$ Wm^{-2}.

In our numerical model, we do not consider wind stress over the domain for simplicity because the correlation between wind stress curl and interannual variations in EOF 2nd mode in the southern part and EOF 1st mode in the northern part of the Japan Sea were low and insignificant (Tables 3.1 to 3.3).

A quasi-steady state is reached at 10 years. First, we compared the seasonal variations in the model result with the observed data for validation (section 4.3), and then the net heat flux was varied to evaluate the effect of surface cooling during winter on the variation in the TBTWC (section 4.4).

4.3 Validation of the model and variability of current paths from winter to summer

We applied EOF analysis to the pressure field of the model result to verify the reproducibility of the seasonal variation in the current pattern. The EOF decomposition of the pressure field yielded two dominant modes explaining 95% and 4% of the total variance. The other modes contributed less than a few percent of the total variance. The spatial patterns and its temporal variations in the first and EOF 2^{nd} modes are shown in Fig. 4.3. Spatial patterns of the EOF 1^{st} and 2^{nd} mode coincided with the result of the EOF analysis of the ASSDH shown in Figs. 3.3a and 3.4a, qualitatively. The time constant of the EOF 1^{st} mode shown in Fig. 4.3b is large from August to November and reaches a maximum in October, but is small from winter to spring in Fig. 4.3b. Characteristics of seasonal variation in the time constant of the EOF 1^{st} mode are almost identical to those in Fig. 4.3c, but the maximum timing shifts by 2 months. The time constant of the EOF 2^{nd} mode is maximum in winter to spring and the minimum in summer to autumn in Fig. 4.3d. The maximum and minimum peak shifts slightly compared to the result of the EOF analysis for the observations shown in Fig. 3.4c. Although the time series of the EOF 1^{st} and 2^{nd} modes have some discrepancies, our model reproduced the seasonal variation in the TWC and subarctic circulation qualitatively.

We investigate variability in the current path using pressure distribution, current velocity, water temperature distribution, and upper layer thickness distribution from winter to summer (Fig. 4.4). Net heat flux was applied by equation (4-10) as the normal year case (NYC). Because a horizontal pressure gradient term can be decomposed horizontal density gradient and horizontal upper layer thickness gradient (McCreary et al., 1997), we can determine which is a more important factor for the current caused by the horizontal density gradient or the horizontal upper layer thickness gradient. In this study, density was defined as a function of water temperature. Therefore, the horizontal density gradient was replaced by the horizontal water temperature gradient.

In winter, sea surface is cooled over the model domain. While warm water is transported by northward flow, the TBTWC occurs along the west coast. Therefore, water temperature in the southern part is warmer than that in the northern part, and a front is formed between the southern and northern parts around x = 50–400, y = 400–600 km (Fig. 4.4b). There is geostrophic flow along the front caused by the horizontal water temperature gradient. This flow transports the coastal water from west coast to offshore. The water transportation causes upward movements of the interface around x = 0–100, y = 400–500 km (Fig. 4.4c). The movements of the interface propagate to the west around x = 0–100, y = 200–500 km as internal Kelvin waves (Fig. 4.4c). As a result, the horizontal interface gradient along the west coast causes a geostrophic flow.

In spring, a positive net heat flux heats the sea surface (Fig. 4.5a). Therefore, the horizontal water temperature gradient becomes gentle, and the geostrophic flow caused by the horizontal water temperature gradient is also weak around x = 0–100, y = 400–600 km (Figs. 4.4b, 4.5b). As the upward movement of the interface is small on the west coast, the geostrophic flow caused by the horizontal interface gradient is weak around x = 0–100, y = 200–500 km (Fig. 4.4a).

In summer, the southward flow, the NCC, is stronger than the TBTWC along the west coast (Fig. 4.5b). Therefore, the NCC intrudes between the west coast and the TBTWC and the separation position of the TBTWC from the coast becomes south (Fig. 4.4a). When the NCC intrudes between the west coast and the TBTWC, a cold-water mass is distributed in the intruded region of the NCC (Fig. 4.4c).

After August, the water temperature gradient between the southern and northern parts is large because the net heat flux is negative (Fig. 4.5a), and the geostrophic flow caused by the water temperature gradient become strong. Therefore, the transportation of the water mass from coast to offshore also increases and causes the internal Kelvin waves along the west coast. Finally, the TBTWC becomes strong (Fig. 4.5b).

4.4 Sensitivity experiments for the winter net heat flux changes

Because the winter net heat flux over the northern Japan Sea seems to control the separation position of the TBTWC from the Koran Peninsula from spring to summer, at first we confirmed the spatial pattern of surface cooling in winter based on observed data. Figure 4.6a shows the difference in net heat flux during winter derived from J-OFURO2 between a strong cooling year (less −270 $\mathrm{Wm^{-2}}$) and a weak cooling year (more −220 $\mathrm{Wm^{-2}}$), respectively. Large differences > 90 $\mathrm{Wm^{-2}}$ distributed along the Russian coast and the difference became smaller toward offshore. Therefore, a step-like pattern of surface cooling shown in Fig. 4.6b was applied to the model and temporal variation in the net heat flux was applied by the following equation:

$$Q_O(t,\mathbf{x}) = Q_m + \{Q_A + Q_{int}(\mathbf{x})\}\sin(2\pi t/T_1 - \pi/2), \qquad (4\text{-}11)$$

$Q_{int}(\mathbf{x})$ is the difference in net heat flux between strong- and weak-cooling years. If $Q_0(t,\mathbf{x}) \geq -100$ $\mathrm{Wm^{-2}}$, $Q_{int}(\mathbf{x}) = 0$. $Q_m = -100$ $\mathrm{Wm^{-2}}$ and, $Q_A = 200$ $\mathrm{Wm^{-2}}$. Figure 10c shows examples of a time series of Q_o at $Q_{int} = 20$, 60, and 100 $\mathrm{Wm^{-2}}$.

Figure 4.7a and b shows pressure and current velocity, and water temperature distributions in the winter, spring, and summer when net heat flux was applied by equation (4-11) as a strong cooling year case (SCYC). In winter, a northward current such as the TBTWC flows along the west coast, then turns to the east around y = 550 km, and meanders toward the eastern end (Fig. 4.7a). The same current pattern is recognized in Fig. 4.4a. However, the difference in the pressure distribution between the

NYC and SCYC indicates a cyclonic circulation pattern in the northern part around x = 50–1000, y = 600–700 km (Fig 4.7c). In spring of SCYC, the northward current along the west coast becomes weaker than that in winter, and the current turns to the east around y = 550 km (Fig. 4.7a). The same current pattern is recognized in Fig. 4.4a in NYC. However, differences in pressure distribution between NYC and SCYC indicate a larger negative anomaly on the western side (Fig. 4.7c). Namely, the subarctic circulation of the SCYC is intensified on the western side compared to that of the NYC, but the separation position of the northward current from the west coast does not change in either case. Strong cooling in winter enhances the subarctic circulation in the spring. This result is supported by the correlation analysis in section 3.3 (Table 3.2). In summer of SCYC, the separation position of the northward flow from the west coast (x = 50, y = 250 km) is more south than that of NYC (Fig. 4.7a). Moreover, the cold-water mass of SCYC intrudes more into the south than that of NYC along the west coast (Figs. 4.4b, 4.7b). This result qualitatively corresponds to the composite water temperature distributions shown in Fig. 3.7. Figure 4.8a and b show the time series of the net heat flux in SCYC and an isoplet of the upper layer thickness difference between SCYC and NYC along the east, north, and west coasts, respectively. Positive anomalies appear in the northeast end (x3) of the domain from December to April, and the anomalies propagate along the north coast. The propagation speed of the anomalies is approximately 1 ms^{-1}, which coincides with the propagation speed of the internal Kelvin wave. From November to April, positive anomalies of upper layer thickness (downward movement of interface) accumulate in the northwestern part by propagation of internal Kelvin waves (Fig. 4.8a). Considering conservation of potential vorticity, the positive vorticity accumulated there due to increase in upper layer thickness. The reason for the accumulation of positive anomalies is that the upward movement of the interface on the west coast, in which the geostrophic flow caused by water temperate gradient transports the water mass from coast to offshore, dissipates propagation of the internal Kelvin wave along the north to west coast.

After April, the TBTWC is weak as similar case of NYC. In spring to summer, enhanced subarctic circulation in SCYC advects the positive anomalies of upper layer thickness and positive vorticity to the south along west coast.

From the above results, the relationship between the change in the separation position of the TBTWC in summer and that of surface cooling in winter is explained as follows. Stronger surface cooling in SCYC increases upper layer thickness along the north coast. The increased upper layer thickness continuously propagates to the west as an internal Kelvin wave. As a result, the upper layer thickness in the western part in

SCYC is deeper than that in NCY. Increased upper layer thickness means a supply of positive vorticity considering conservation of potential vorticity. Hence, the subarctic circulation in spring is intensified, as shown in Fig. 4.7c. The intensified subarctic circulation transports the positive vorticity to the south along the west coast. Because southward flow along the west coast in SCYC is faster than that in NCY, deeper upper layer thickness expands more to the south in summer. Consequently, the northward current (TBTWC) along the west coast in the SCYC separates at a lower latitude than that in NCY.

4.5 Summary

We examined the mechanism of the interannual variation in the TBTWC path by means of a reduced gravity model with simple topography. The reduced gravity model reproduces seasonal variation in the TWC and subarctic circulation qualitatively. We carried out two cases of numerical experiments with different cooling conditions; i.e., a normal cooling year (NCY) case and a strong cooling year (SCYC) case to understand the influence of surface cooling in winter to variations of TBTWC and subarctic circulation. Strong cooling in winter enhanced subarctic circulation in the spring. This result was consistent with the correlation analysis of the ASSDH data and the net heat flux data. In summer of SCYC, the separation position of the northward flow (TBTWC) from the west coast was more south than that of NYC. Moreover, a cold-water mass of the SCYC intruded more to the south than that of NYC along the west coast. This result qualitatively corresponded to the composite water temperature distributions.

Comparing the upper layer thickness in SCYC with that in NYC, positive anomalies appeared in the northeast end of the domain from November to April, and the anomalies propagated along the north coast as an internal Kelvin wave. The propagation of internal Kelvin waves supplied positive vorticity on the west side and resulted in intensification of subarctic circulation in the spring in SCYC. The intensified southward current (North Korean Cold Current) of SCYC, which is a part of the subarctic circulation, transported the positive vorticity to the south. Consequently, the northward current (TBTWC) along the west coast in summer in SCYC separates at lower latitudes than that of the NCY.

In the present model study, we did not consider wind stress over the Japan Sea because there was no significant correlation between interannual variations in the TBTWC and wind stress curl. However, previous studies reported that the subarctic circulation is influenced by the wind stress curl (Yoon et al., 2005; Kim and Yoon, 2010). In addition, our model results suggest that intensification of the subarctic circulation enhances transport of positive vorticity to the south. Therefore, we should consider wind stress over the Japan Sea to investigate further the detailed mechanism of interannual variation in the TBTWC path. In fact, Hogan and Hurlburt (2005) pointed out that the choice of the wind data in the Japan Sea is an important factor in determining the separation position of the TBTWC from the coast. Hence, we will investigate the effect of wind stress to the TBTWC path variation in the near future.

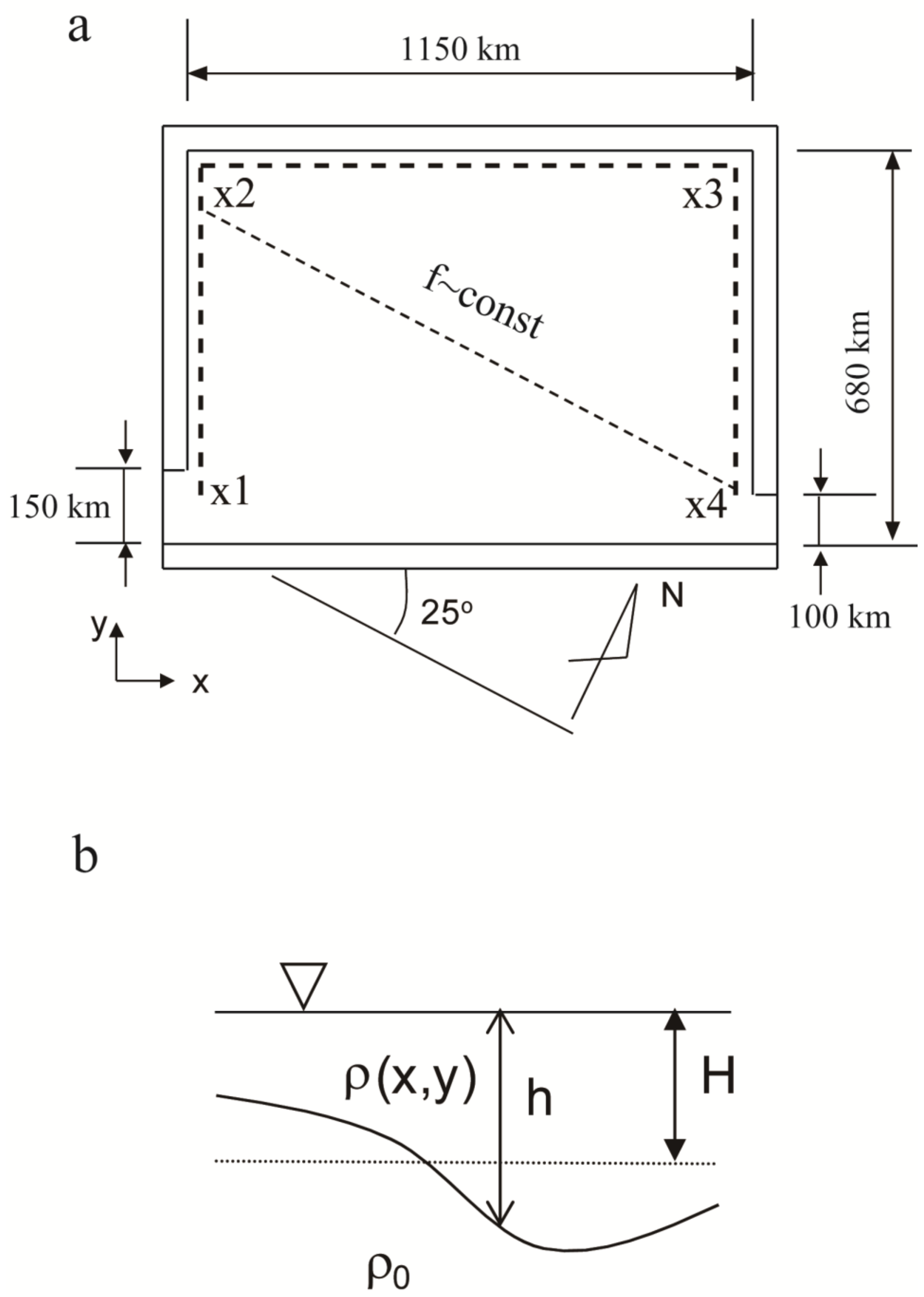

Figure 4.1: (a) Schematic representation of the model ocean. Thick and thin dashed lines represent the x axis of Fig. 4.8 and the direction of co-Colioris parameter, respectively. (b) Schematic representation of the reduced gravity model. The ρ_0 and ρ denote the density of the lower and upper layers, respectively. H is the upper layer thickness at rest. The h is the upper layer thickness.

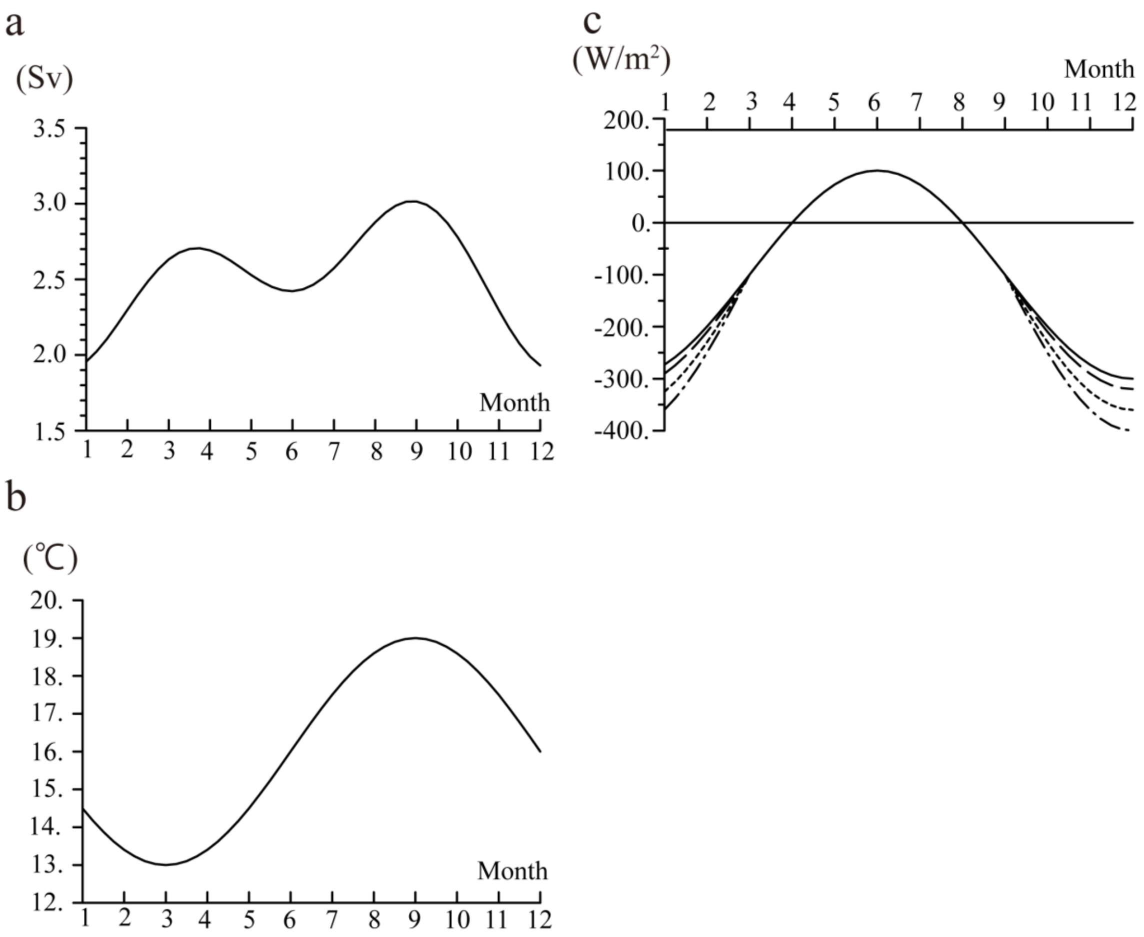

Figure 4.2: Open boundary condition of (a) volume transport and (b) water temperature at the southwestern channel (Tsushima Strait). (c) Surface boundary condition of net heat flux. Solid, long dashed, dashed, and dashed-dotted lines represent seasonal variations of net heat flux in the case of $Q_{int} = 0$, 20, 60 and 100 Wm^{-2}, respectively.

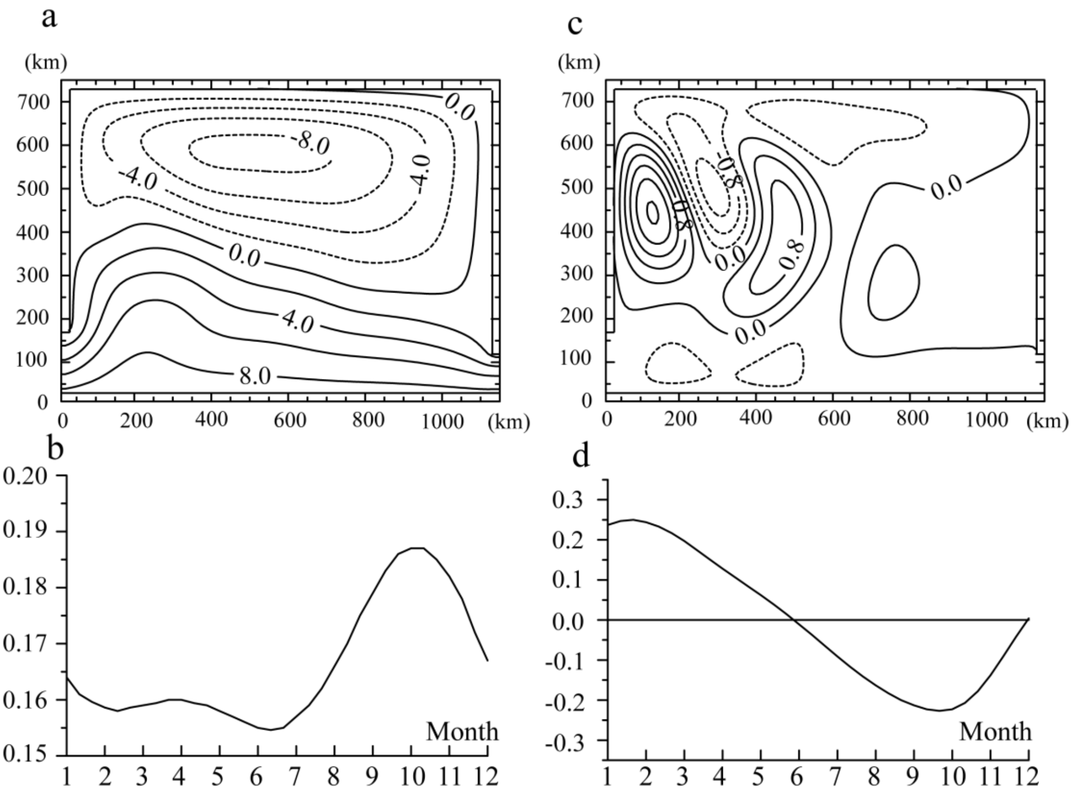

Figure 4.3: Empirical orthogonal function (EOF) 1st and 2nd modes of pressure field: (a) spatial structure of EOF 1st mode, (b) temporal variation of time constant of EOF 1st mode (×100 m^3s^{-2}), (c) spatial structure of EOF 2nd mode, and (d) temporal variation of time constant of EOF 2nd mode (×200 m^3s^{-2}).

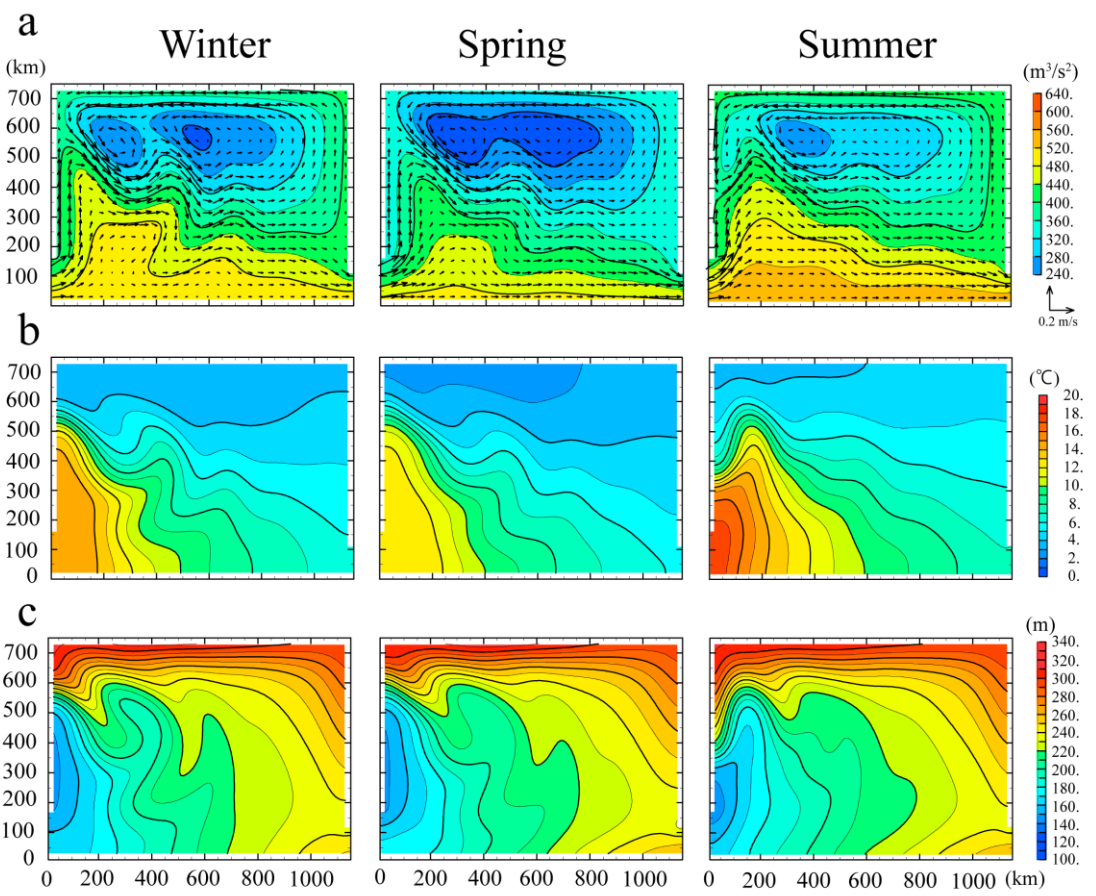

Figure 4.4: Distributions of (a) pressure and current velocity, (b) water temperature, and (c) upper layer thickness in winter (January), spring (April), summer (July) in the case of NCY.

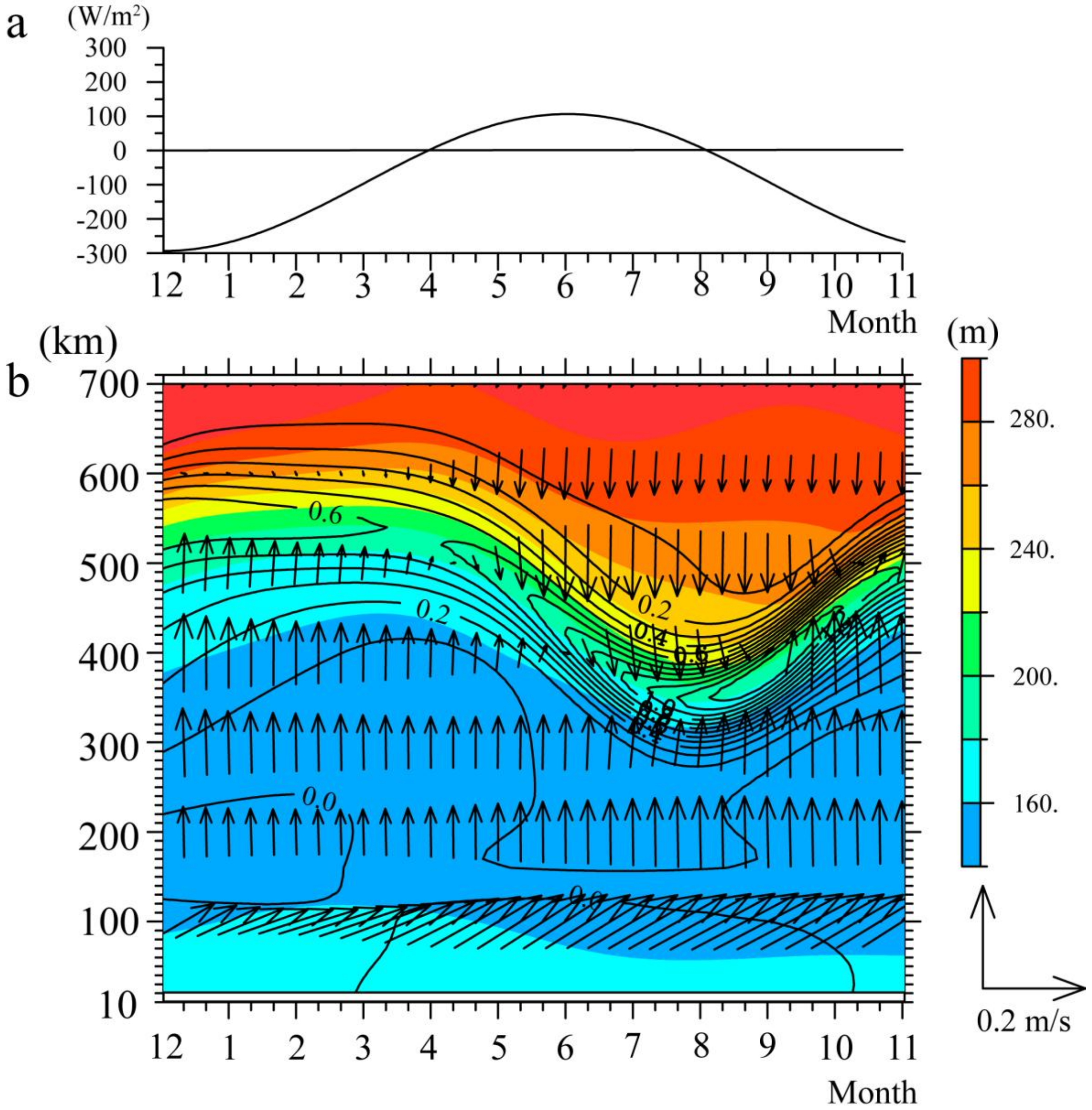

Figure 4.5: (a) Time series of the net heat flux in the model. (b) Isoplet diagram of upper layer thickness of the NCY along the western boundary in the model. Shade indicates the upper layer thickness. Contours indicate the horizontal water temperature gradient ($\times 10^{-1}$°C km^{-1}). The vectors indicate the current velocity.

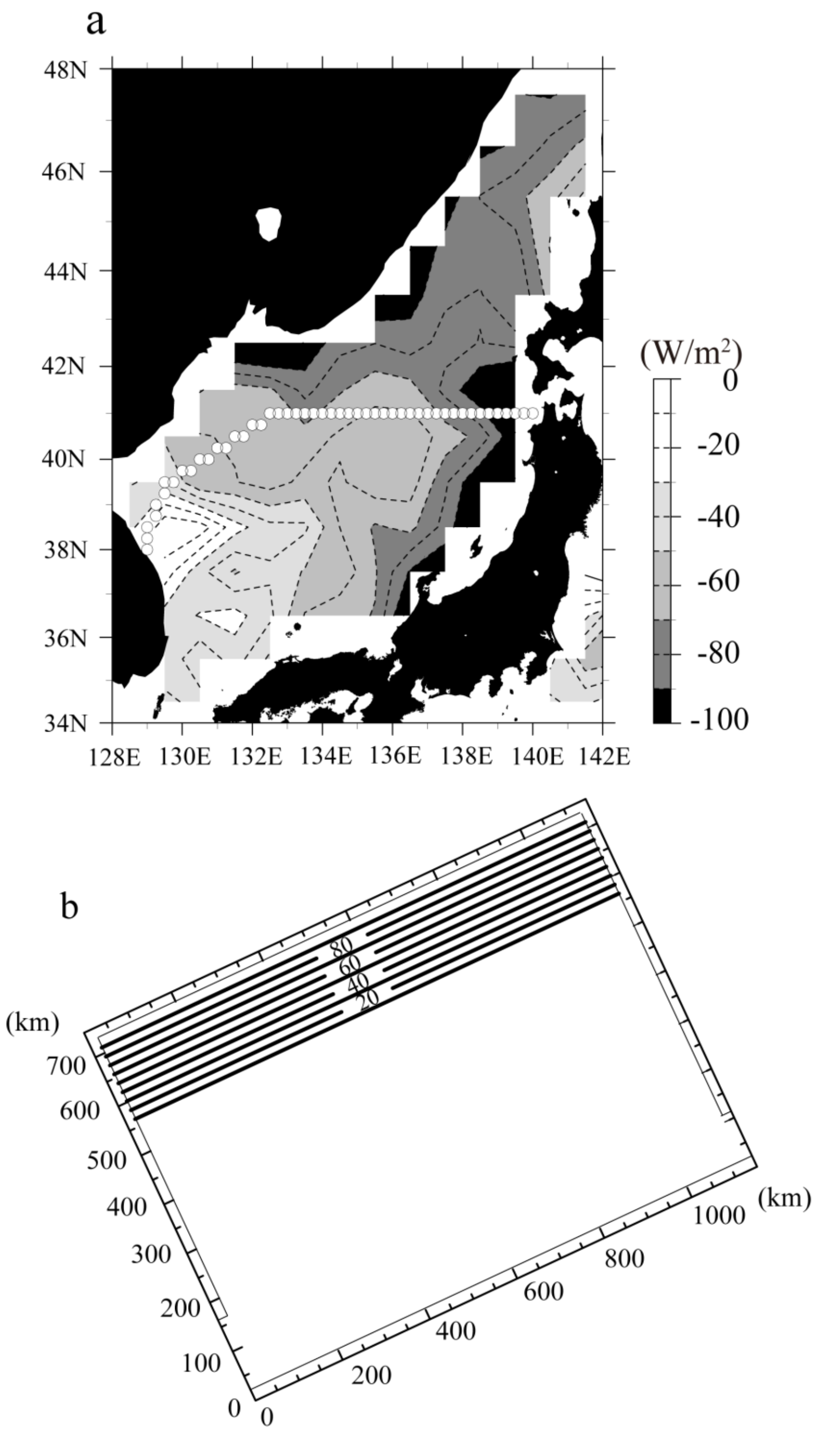

Figure 4.6: Difference of (a) net heat flux in winter derived from J-OFURO 2 between strong cooling (less −270 Wm^{-2}) and weak cooling (more −220 Wm^{-2}) years. The contours and shades indicate the net heat flux difference. White circles indicate the boundary between the southern and northern part of the Japan Sea. (b) Spatial distribution of Q_{int} in equation (4-11). Contours indicate Q_{int} (Wm^{-2}).

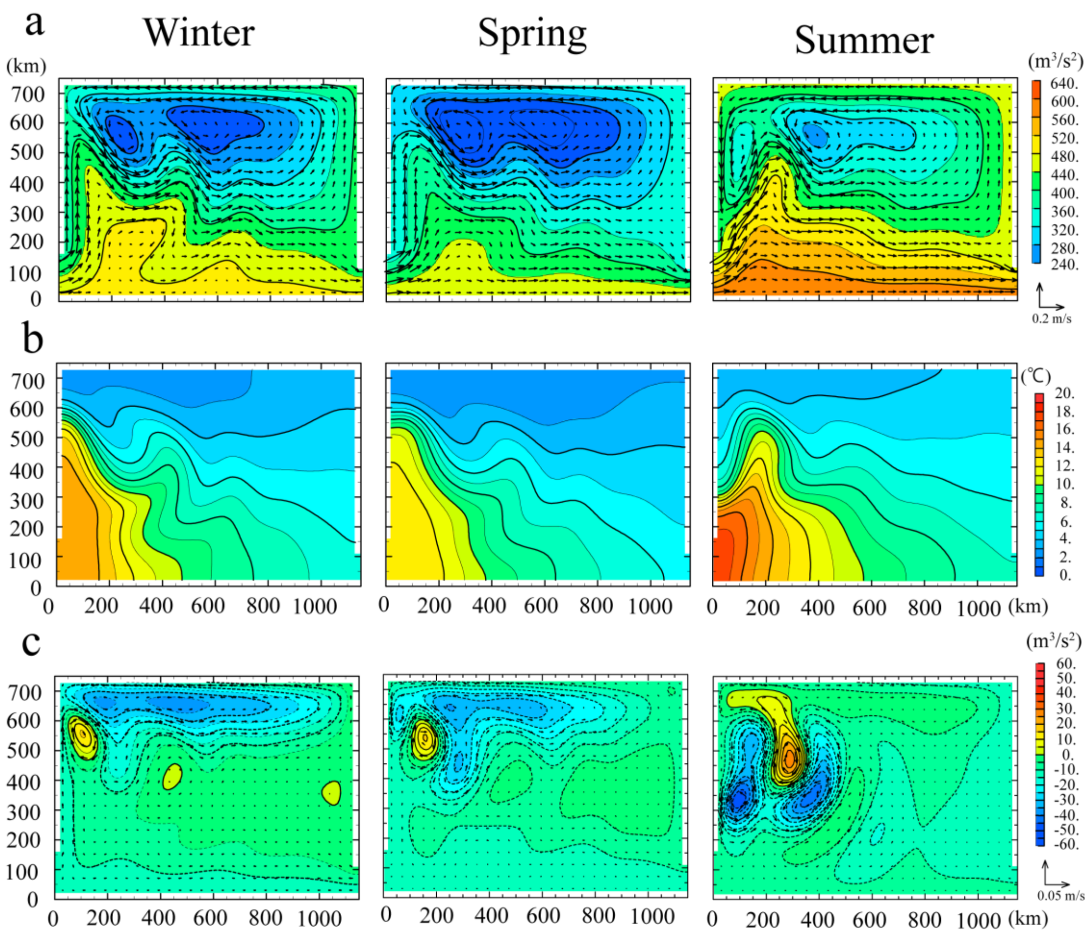

Figure 4.7: Distributions of (a) pressure and current velocity, and (b) water temperature in winter (January), spring (April), summer (July) in the case of SYCY. (c) Differences of pressure and current velocity between NCY and SCYC in winter (January), spring (April), and summer (July).

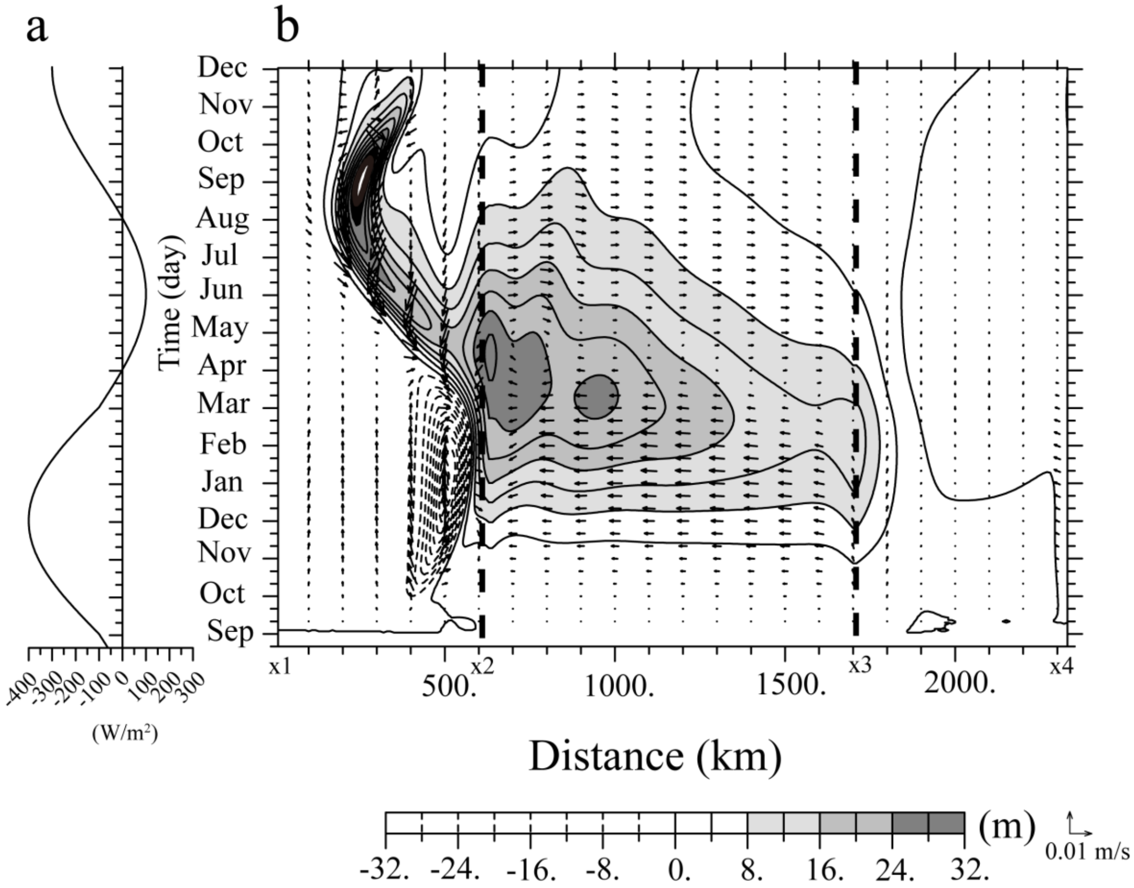

Figure 4.8: (a) Time series of the net heat flux when Q_{int} equals 100 Wm^{-2}. (b) Isoplet diagram of the difference in upper layer thickness between NCY and SCYC. Contours and shade indicate the difference in layer thickness. The vectors indicate the difference in current velocity. Dashed lines indicate the position of x2 and x3 shown in Fig. 4.1a.

Chapter 5

General Discussion

The Tsushima Warm Current (TWC) flows into the Japan Sea through the Tsushima Strait with shallow water depth. The TWC encounters an abrupt water depth change from 100 m to more than 1500 m depth in the southwestern part of the Japan Sea after passing through the Tsushima Strait. The Branching of the TWC path associated with the abrupt water depth change in the southwestern part of the Japan Sea have been investigated since 1980s. Previous studies suggested that a current is trapped by continental shelf edge and the other current flows along the Korea Peninsula due to the planetary β effect. Several current paths are proposed based on observed water temperature and snapshots current velocity data and numerical models.

In the present study, a mean current path, seasonal and interannual variation in the TWC paths in the southwestern part of the Japan Sea were investigated using sea surface dynamical height and absolute sea surface current field data with high spatiotemporal resolution. It was revealed that there are three current paths in the southwestern part of the Japan Sea. First branch of the TWC (FBTWC) flows northward along shallow isobaths around Japanese archipelago throughout the year. Second branch of the TWC (SBTWC) flows along continental shelf edge with seasonal variation. Third branch of the TWC (TBTWC) flows along the Korean Peninsula with seasonal and interannual variations.

Kawabe (1982b) showed from a numerical model experiment that the SBTWC is formed by continental shelf waves associated with increasing a volume transport in the Tsushima Strait. However, the SBTWC exists in all months except November, and clear relationship between formation of the SBTWC and change of volume transport of the TWC was not recognized. This fact suggests that the SBTWC is sustained by not only continental shelf waves but also other mechanisms. A numerical model result reconstructing circulations around the southwestern part of the Japan Sea by Kim et al. (2009) advances understandings of a reason of the sustaining SBTWC path. According to their model result, upper part of the North Korean Cold Current (NCC), which flows southward along the east coast of the Korean Peninsula, encounters the TBTWC and lower part of the NCC flows along the continental shelf edge around the San’in coast. It is possibility that the NCC transported the lower temperature water mass from the northern part of the Japan Sea and sustained the baroclinity around the continental shelf edge where the SBTWC flows. If the NCC was strength by the winter surface cooling in the northern part of the Japan Sea, much lower temperature water mass was transported by the NKCC rather than normal winter surface cooling. As a result, intensification of the SBTWC is considered. Since there is no volume transport data of the SBTWC, we cannot examine the above mentioned at the moment.

The TBTWC has been considered a western boundary current with stable current path from numerical model results (Kawabe, 1982a,b; Yoon, 1982). However, the TBTWC path had high variability in the southwestern part of the Japan Sea as shown in chapters 2, 3, and 4. The TBTWC is generated by transportation of kinematic energy toward westward by the Rossby waves (Sekine, 1989), and the current is considered as a weaker western boundary current than that driven by wind-driven circulation. Therefore, the TBTWC path might have large interannual variation, and separation position of the TBTWC from the Korean Peninsula in summer might be controlled by the winter surface cooling in the northern part of the Japan Sea.

In chapter 3 and 4, variation in the TBTWC was qualitatively clarified by influence of the winter surface cooling. Another effect of the winter surface cooling to the TWC system is a Cooling-Induced Current system proposed by Isoda (1999). Cooling-Induced Current system is explained as follows. Yearly averaged net heat flux in the Japan Sea is negative (cooling the sea surface) and permanent polar front exists.

Warm water mass must be transported from the Tsushima Strait in order to sustain the polar front. Based on Cooling-Induced Current system, when amount of cooling in the Japan Sea is large, large amount of warm water is supplied through the Tsushima Strait. Therefore, the variation of the volume transport in the Tsushima Strait is caused by the cooling in the Japan Sea. There is a possibility that increase and decrease of the volume transport through the Tsushima Strait strengthens the TBTWC and changes the variation of the TBTWC path. However, there is no significant relation of variations between the TBTWC path explained by EOF 2nd mode in chapter 3 and volume transport through the Tsushima Strait. This may be because Isoda (1999) used a box model and did not consider the circulation such as the TBTWC and a current along polar front. Although we calculated the correlation coefficient between the net heat flux over the Japan Sea, northern part of the Japan Sea and volume transport through the Tsushima Strait, we did not see the significant correlation between them. It is considered that driving mechanism of the TWC is not only Cooling-Induced Current System but also difference of dynamical sea surface height between East China Sea and eastern part off the Tsugaru Strait (Toba et al., 1982).

It is difficult to carry out the observation around maritime border and severe weather condition in winter time. However, in the future many of observation data and sea surface height data might be accumulated by development of observation techniques such as remote sensing, and we might be able to reveal the TWC paths and those variations not only in the southwestern part of the Japan Sea but also in the entire Japan Sea.

Chapter 6

Conclusion

In order to reveal variability in the TWC path, we made the absolute sea surface current field and absolute sea surface dynamic height field data with high special and temporal resolution and investigated the current path pattern. The triple-branch current path pattern was shown in the southwestern part of the Japan Sea. Moreover, we investigated the seasonal variation of the TWC path by using a stability index which was calculated by frequency of current direction and standard deviation. The FBTWC through the eastern channel of the Tsushima Strait flows along the Japanese archipelago in all months as a highly stable current. The TBTWC through the western channel of the Tsushima Strait flows along the east coast of the Korean peninsula in all months and is also classified as highly stable. Two current paths separate from the TBTWC around 38°N, 130°E. The southeastward current is stable in June, September, and December. The northeastward current is also stable from June to February except in January. The SBTWC west of 131°E flows as a stable current throughout the year except in November. East of 131°E, the offshore current path appears as a highly stable current in all months. This current path originates from the SBTWC, and the FBTWC might bifurcate after passing north of Mishima Island, and then southward flow may arise in the north. The nearshore current path originates from the FBTWC.

To reveal the variability in the TWC paths, EOF analysis was carried out with use of the absolute sea surface dynamic height (ASSDH) in the southern Japan Sea. The EOF 1st mode of ASSDH variation explained 79% and the EOF 2nd mode explained 9% of the total variance. Spatial distribution of 1st mode was similar to that of mean sea surface height and reflected the current path pattern of TWC from the Tsushima Strait to Tsugaru Strait. The time constant of 1st mode showed positive values, and annual cycle was dominant. As for spatial variance of EOF 2nd mode, three large amplitude areas were recognized. The time constant of EOF 2nd mode showed interannual variation was dominant. Most large amplitude area was east off Korean Peninsula and the variations influenced to interannual variations in separation position of the TBTWC from the Korean Peninsula of the TBTWC path.

Monthly averaged time constants of EOF 2nd mode from spring to summer correlated with surface cooling in winter averaged in the northern part of the Japan Sea. This result suggested that interannual variation of separation position of the TBTWC from spring to summer is caused by that of surface cooling in winter in the northern part of the Japan

Sea. EOF 1st mode of the ASSDH in the northern part of the Japan Sea, which denotes strong and weak of the Liman Cold Current, also has high correlation with surface cooling in winter averaged in the northern part of the Japan Sea. Correlation analyses suggested that interannual variation of the TBTWC, especially separation position of the TBTWC from the Korean Peninsula, relates to strong and weak variation of the Liman Cold Current. In addition, strong and weak of Liman Cold Current in spring might be caused by variation in surface cooling in winter.

In order to reveal the relationship between variation in strength of surface cooling in winter and that in the TBTWC path pattern from spring to summer, especially the separation position of the TBTWC from the Koran peninsula, we carried out numerical experiment by mean of the reduced gravity model. The reduced gravity model could reproduce seasonal variation of the TBTWC and subarctic circulation qualitatively. In order to understand influence of surface cooling in winter to the variations of TBTWC and subarctic circulation, we carried out two case of numerical experiments with difference cooling condition, normal cooling year case and strong cooling year case. It was found that strong cooling in winter enhances subarctic circulation in spring. The result was consistent with correlation analysis of the ASSDH data and net heat flux data. In summer of strong cooling year case, the separation position of the TBTWC from the west coast was more south than that of normal cooling year case.

Comparing upper layer thickness in strong cooling year case with that in normal cooling year case, positive anomalies appears in the northeast end of model domain from December to May, and the anomalies propagate along north coast as internal Kelvin wave. The propagation of internal Kelvin waves supplies positive vorticity in the west side and result in intensification of subarctic circulation in spring in strong cooling year case. Intensified southward current of strong cooling year case which is a part of the subarctic circulation transports the positive vorticity to the south. Consequently, the northward current (TBTWC) along west coast in summer in strong cooling year case separates at lower latitude than that in normal cooling year case.

References

Ambe, D., S. Imawaki, H. Uchida, and K. Ichikawa, 2004. Estimating the Kuroshio axis south of Japan using combination of satellite altimetry and drifting buoys. Journal of Oceanography **60**, 375–382.

AVISO, 2008. DT-CorSSH and DT SLA Product Handbook, CLS-DOS-NT-08.341.

Blumberg, A.F., G.L. Mellor, 1987. A description of a three dimensional coastal ocean circulation model. In: Heaps, N.S. (Ed.), Three-Dimensional Coastal Ocean Models. Coastal and Estuarine Sciences, **4**, 1-16.

Centurioni, R.L., P.N. Niiler, and D.K. Lee, 2009. Near-surface circulation in the South China Sea during the winter monsoon. Geophysical Research Letters. **36**, L06605. http://dx.doi.org/10.1029/2008GL037076.

Choi, B.J., D.B. Haidvogel, and Y.K. Cho, 2009. Interannual variation of the Polar Front in the Japan/East Sea from summertime hydrography and sea level data. Journal of Marine Systems, **78**, 351-362.

Davey, M.K., 1983. A two-level model of a thermally forced ocean basin. Journal of Physical Oceanography, **13**, 196-190.

Hansen, D.V., P.M. Poulain, 1996. Quality control and interpolation of WOCE/TOGA drifter data. Journal of Atmospheric and Oceanic Technology. **13**, 900–909.

Hase, H., J.H. Yoon, and W. Koterayama, 1999. The current structure of the Tsushima Warm Current along the Japanese Coast. Journal of Oceanography. **55**, 217–235.

Hirose, N., R. Kobayashi, and K. Takayama, 2009. Validation of the number of branches in the Tsushima Warm Current based on assimilated estimates. Umi to Sora. **85**, 25–35 (in Japanese with English abstract).

Hong, C.H., K.D. Cho, 1983. The northern boundary of the Tsushima current and its fluctuations. Journal of the Oceanographical Society of Korea, **18**, 1-9.

Hogan, L.J., H.E. Hurlburt, 2000. Impact of upper ocean-topographical coupling and isopycnal outcropping in Japan/East Sea models with 1/8 to 1/64 resolution. Journal of Physical Oceanography. **30**, 2535–2561.

Hogan, P.J., H.E. Hurlburt, 2005. Sensitivity of simulated circulation dynamics to the choice of surface wind forcing in the Japan/East Sea. Deep Sea Research II, **52**, 1464-1489.

Imawaki, S., K. Ichikawa, and H. Nishigaki, 1991. Mapping the mean sea surface elevation field from satellite altimetry data using optimal interpolation. Marine Geodesy. **15**, 31–46.

Isobe, A., M. Ando, T. Watanabe, and T. Senjyu, 2002. Freshwater and temperature transports through the Tsushima – Korea Straits. Journal of Geophysical Research Oceans. **107**. http://dx.doi.org/10.1029/2000JC000702.

Isoda, Y., T. Murayama, 1990. Bottom cold water and the flow structure of the Tsushima Warm Current off Hamada. Bulletin on Coastal Oceanography 28, 85–95 (in Japanese with English abstract).

Isoda, Y., S. Saitoh, 1993. The northward intruding eddy along the east coast of Korea. Journal of Oceanography. **49**, 443–458.

Isoda, Y., 1994. Warm Eddy movements in the eastern Japan Sea. Journal of Oceanography. **50**, 1–15.

Isoda, Y., 1999. Cooling-Induced Current in the Upper Ocean of the Japan Sea. Journal of Oceanography. **55**, 585–596.

Katoh, O., 1993. Detailed current structures over the continental shelf off the San’in Coast in summer. Journal of Oceanography. **49**, 1–16.

Katoh, O., 1994a. Short-term fluctuations of the Tsushima Current in waters northwest of Yamaguchi Prefecture. Journal of Oceanography. **50**, 51–64.

Katoh, O., 1994b. Structure of the Tsushima Current in the Southwestern Japan Sea. Journal of Oceanography. **50**, 317–338.

Kawabe, M., 1982a. Branching of the Tsushima Current in the Japan Sea part I. Data analysis. Journal of the Oceanographical Society of Japan. **38**, 95–107.

Kawabe, M., 1982b. Branching of the Tsushima Current in the Japan Sea part II. Numerical experiment. Journal of the Oceanographical Society of Japan. **38**, 183–192.

Kawase, M., 1987. Establishment of deep ocean circulation driven by deep-water production. Journal of Physical Oceanography, **17**, 2294-2317.

Kim, Y.H., K.I. Chang, J.J. Park, S.K. Park, S.H. Lee, Y.G. Kim, and K.T. Jung, 2009. Comparison between a reanalyzed product by 3-dimensional variational assimilation technique and observations in the Ulleung Basin of the East/Japan Sea. Journal of Marine Systems, **78**, 249-264.

Kim, K., R. Legeckis, 1986. Branching of the Tsushima Current in 1981-83. Progress in Oceanography. **17**, 265-276.

Kim, C.H., K. Kim, 1983, Characteristics and origin of the cold water mass along the east coast of Korea, The Journal of the Oceanological Society of Korea, **18**, 73-83. (in Korea with English abstract)

Kim, C.H., J.H. Yoon, 1996, Modeling of the Wind-Driven Circulation in the Japan Sea Using a Reduced Gravity Model. Journal of Oceanography, **52**, 359-373.

Kim, T., J.H. Yoon, 2010. Seasonal variation of upper layer circulation in the northern part of the East/Japan Sea. Continental Shelf Research, **30**, 1283-1301.

Lagerloef, G.S.E., R.L. Bernstein, 1988. Empirical orthogonal function analysis of advanced very high resolution radiometer surface temperature patterns in Santa Barbara Channel. Journal of Geophysical Research, 93, doi:10.1029/88JC01526.

Lee, D.K., P.P. Niiler, 2005. The energetic surface circulation patterns of the Japan/East Sea. Deep-Sea Research Part II, **52**, 1547–1563.

Lee, D.K., P.P. Niiler, 2010a. Surface circulation in the southwestern Japan/East Sea as observed from drifters and sea surface height. Deep-Sea Research Part I, **57**, 1222–1232.

Lee, D.K., P.P. Niiler, 2010b. Eddies in the southwestern East/Japan Sea. Deep-Sea Research Part I, **57**, 1233–1242.

Lie, H.J., 1991. COASTAL CURRENT AND ITS VARIATION ALONG THE EAST COAST OF KORA. JECCSS, ed. by K.Takano, Elsevier, 399-408.

McCreary Jr, J.P., S. Zhang, 1997. Coastal circulations driven by river out flow in a variable-density 1 1/2-layer model. Journal of Geophysical Research, **102**, 535-554.

Mooers, N.H.C., H. Kang, I. Bang, and D.P. Snowden, 2006. Some lessons learned from comparisons of numerical simulations and observations of the JES circulation. Special Issue on the Japan/East Sea, Journal of Oceanography, **19**, 86–95.

Morimoto, A., T. Yanagi, and A. Kaneko, 2000. Eddy field in the Japan Sea derived from satellite altimetric data. Journal of Oceanography, **56**, 449–462.

Morimoto, A., T. Yanagi, 2001. Variability of sea surface circulation in the Japan Sea. Journal of Oceanography, **57**, 1–13.

Morimoto, A., 2009. Evaluation of tidal error in altimetry data in the Asian marginal seas. Journal of Oceanography, **65**, 477–485.

Morimoto, A., Y. Isoda, T. Tameishi, and S. Moriwaki, 2009a. Seasonal variation in Tsushima Warm Current paths over the shelf off the San'in coast, Japan. Continental Shelf Research, **29**, 1437–1447.

Morimoto, A., T. Takikawa, G. Onitsuka, A. Watanabe, M. Moku, and T. Yanagi, 2009b. Seasonal variation of horizontal material transport through the eastern channel of the Tsushima straits. Journal of Oceanography, **65**, 61–71.

Moriwaki, S., Y. Ogawa, 1988. Hydrographic features of the ‘‘bottom cold water’’ on the continental shelf. Bulletin on Tohoku Regional Fisheries Research Laboratory, **50**, 25–47 (in Japanese with English abstract).

Moriwaki, S., Y. Ogawa, 1989. Influences of the ‘‘Bottom Cold Water’’ on demersal fishes in the Southwestern Japan Sea. Bulletin on Tohoku Regional Fisheries Research Laboratory, **51**, 167–181 (in Japanese with English abstract).

Mitchell, D.A., D.R. Watts, M. Wimbush, W.J. Teague, K.L. Tracey, J.W. Book, K.I. Chang, M.S. Suk, and J.H. Yoon, 2005. Upper circulation patterns in the Ulleung Basin. Deep-Sea Research Part II, **52**, 1617–1638.

Naganuma, K., 1985. Fishing and Oceanographic conditions in the Japan Sea. Umi to Sora, **60**, 89-103 (in Japanese)

Ogawa, Y., S. Moriwaki, 1986. A possible mechanism of fluctuations of socalled ‘‘Bottom Cold Water’’ on the continental shelf. Bulletin on Tohoku Regional Fisheries Research Laboratory, **48**, 97–114 (in Japanese with English abstract).

Onitsuka, G., T. Yanagi, and J.H. Yoon, 2007. A numerical study on nutrient sources in the surface layer of the Japan Sea using a coupled physical-ecosystem model. Journal of Geophysical Research Oceans, **112**, http://dx.doi.org/10.1029/2006JC003981.

Onogi, K., J. Tsutsui, H. Koide, M. Sakamoto, S. Kobayashi, H. Hatsushika, T. Matsumoto, N. Yamazaki, H. Kamahori, K. Takahashi, S. Kadokura, K. Wada, K. Kato, R. Oyama, T. Ose, N. Mannoji, and R. Taira, 2007. The JRA-25 reanalysis. Journal of Meteorological Society of Japan, **85**, 369–432.

Sekine, Y., 1986. Wind-driven circulation in the Japan Sea and its influence on the branching of the Tsushima Current. Progress in Oceanography, **17**, 297–312.

Senjyu, T. 1999. The Japan Sea Intermediate Water; Its Characteristics and Circulation. Journal of Oceanography, **55**, 111-122.

Seung, Y.H., K. Kim, 1989. On the Possible Role of Local Thermal Forcing on the Japan Sea Circultaion. Journal of the Oceanographical Society of Korea, **24**, 29-38.

Seung, Y.H., S.Y. Nam, 1991. EFFECT OF WINTER COOLING ON SUBSURFACE HYDROGRAPHIC CONDITIONS OFF KOREAN COAST IN THE EAST (JAPAN) SEA. JECCSS, ed. by K.Takano, Elsevier, 163-178.

Seung, Y.H., 1992. A Simple Model for Separation of East Korean Warm Current and Formation of North Korean Cold Current. The Journal of the Oceanological Society of Korea, **27**, 189-196.

Tanioka, K., 1968. On the East Korean Warm Current (Tosen Warm Current). The Oceanographical Magazine, **20**, 31–38.

Takikawa, T., J.H. Yoon, 2005. Volume transport through the Tsushima straits estimated from sea level difference. Journal of Oceanography, **61**, 699–708.

Toba, Y., K. Tomizawa, Y.Kurasawa and K. Hanawa, 1982. Seasonal and interannual variability of the Tsushima – Tsugaru Warm Current System with its possible cause. La mer, **20**, 40-51.

Tomita, H., Kubota. M., Cronin, M.F., Konda. M., Ichikawa. H., 2010. An assessment of surface heat fluxes from J-OFURO2 at the KEO/JKEO sites. Journal of Geophysical Reseach., 115,C03018,doi:10.1029/2009JC005545.

Uchida, H., S. Imawaki, 2003. Eulerian mean surface velocity field derived by combining drifter and satellite altimeter data. Geophysical Research Letters, **30**, http://dx.doi.org/10.1029/2002GL016445.

Uda, M., 1934a. The results of simultaneous oceanographical investigations in the Japan Sea and its adjacent waters in May and June, 1932. Japan Imperial Fishery Experiment Stations, **5**, 57–190 (in Japanese).

Uda, M. 1934b. Hydrographic researches on the normal monthly conditions in the Japan Sea, the Yellow Sea and the Okhotsk Sea. Jour. Imp. Fish. Exp. St. **5**, 191-193.

Uda, M. 1936. Results of simulataneous oceanographic investigations in the Japan Sea and its adjacent waters during October and November, 1933. Jour. Imp. Fish. Exp. St., **7**, 150-178.

Watanabe, T., D. Simizu, K. Nishiuchi, T. Hasegawa, and O. Katoh, 2009. Surface current structure of the Tsushima Warm Current region in the Japan Sea derived by satellite-tracked surface drifters. Journal of Oceanography, **65**, 791–801.

Watts, D.R., M. Wimbush, K.L. Tracey, W.J. Teague, J.H. Park, D.A. Mitchell, J.H. Yoon, M.S. Suk, and K.I. Chang, 2006. Currents, eddies, and a ‘‘Fish Story’’ in the southwestern Japan/East Sea. Special Issue on the Japan/East Sea. Journal of Oceanography, **19**, 64–75.

Yamazaki, S., 1969. ‘‘Bottom Cold Water’’ on the continental shelf. Bulletin on Japanese Society of Fisheries Oceanography, **48**, 93–101 (in Japanese).

Yarichin, V.G., 1980. Status of the research of the Japan Sea water circulation. Trudy DVNIGMI, **80** , 46-61.

Yoon, J.H. 1982. Numerical experiment on the circulation in the Japan Sea, Part I formation of the East Koran Warm Current. Journal of the Oceanographical Society of Japan, **38**, 43-51.

Yoon, J.H., K. Abe, T. Ogata, and Y. Wakamatsu, 2005. The effect of wind-stress curl on the Japan /East Sea circulation. Deep Sea Research II, **52**, 1827-1844.

Yun, J.Y., L. Maggard, K. Kim, C.W. Shin, C. Kim, and S.K. Byun, 2004. Spatial and temporal variability of the North Korean Cold Water leading to the near-bottom cold water intrusion in Korea Strait, Progress in Oceanography, **60**, 99-131.